UNIVERSITY OF KWAZULU-NATAL

Southern African Large Telescope Observations of Sunyaev-Zel'dovich Effect Selected Clusters from the Atacama Cosmology Telescope

by

Brian Kirk

Submitted in fulfillment of the
academic requirements for the degree of
Master of Science,
in the
School of Mathematics, Statistics, and Computer Science,
University of KwaZulu-Natal

Durban
May 2014

By the supervisors

As the candidate's supervisors we agree to the submission of this dissertation.

Signed:

Dr Matt Hilton   Prof Catherine Cress

Date: 19 May 2014

By the candidate

I, Brian Kirk, declare that

i) The research reported in this dissertation, except where otherwise indicated, is my original work.

ii) This dissertation has not been submitted for any degree or examination at any other university.

iii) This dissertation does not contain other persons' data, pictures, graphs or other information, unless specifically acknowledged as being sourced from other persons.

iv) This dissertation does not contain other persons' writing, unless specifically acknowledged as being sourced from other researchers. Where other written sources have been quoted, then:

    a) their words have been re-written but the general information attributed to them has been referenced;

    b) where their exact words have been used, their writing has been placed inside quotation marks, and referenced.

v) Where I have reproduced a publication of which I am an author, co-author or editor, I have indicated in detail which part of the publication was actually written by myself alone and have fully referenced such publications.

vi) This dissertation does not contain text, graphics or tables copied and pasted from the Internet, unless specifically acknowledged, and the source being detailed in the dissertation and in the References sections.

Signed:

Brian Kirk

Brian Kirk

Date: 19 May 2014

Abstract

We present Southern African Large Telescope (SALT) follow-up observations of seven massive clusters detected by the Atacama Cosmology Telescope (ACT) using the Sunyaev-Zel'dovich effect (SZE). We conducted multi-object spectroscopic observations with the Robert Stobie Spectrograph (RSS) in order to measure galaxy redshifts in each cluster field, determine the cluster line of sight velocity dispersions, and infer the cluster dynamical masses. This programme forms part of the larger ACT effort to measure the SZE-signal-to-mass relation using a mass proxy which is independent of cluster gas properties. While all of the clusters in this work have previously been identified in optical surveys within the Sloan Digital Sky Survey footprint, none of them have been studied in this way before. We find that the clusters range in mass from $(0.26 - 2.6) \times 10^{15}$ M$_\odot$ and span the redshift range $0.3 < z < 0.55$. The spectrum of the Brightest Cluster Galaxy (BCG) in ACT-CL J0320.4+0032 shows strong emission line features indicating the presence of an Active Galactic Nucleus (AGN), potentially providing feedback within a very massive cluster.

Contents

List of Tables

List of Figures

x

Introduction

1.1 Introduction to Cosmology

In this work, clusters of galaxies are studied with a view to use them for cosmological studies. In the first section, I outline the standard cosmological framework, discussing observations that can be used to test and refine the model. The second chapter focuses on previous observations that use clusters of galaxies as a probe of cosmology and motivates the study described in Chapter 3. Data from the Southern African Large Telescope is then presented and analyzed, leading to the discussion in Chapter 4, where we compare our results with previous work and discuss the relevance for future studies.

The discipline of cosmology is the study of the Universe as a whole. Physical laws dictate the evolution of the Universe, allowing us to understand its past and predict its future. The first set of descriptive equations about the Universe came from Einstein's General Theory of Relativity. Einstein assumed the Universe was unchanging in time and in his equations, to counter-balance the attractive force of gravity, he introduced a term to represent a sort of "anti-gravity". He called

the term the "cosmological constant" and nowadays it is typically represented by lambda, or Λ.

Shortly after, Friedmann solved Einstein's equations (Friedmann, 1924), without the assumption of a static Universe, and produced a set of equations in which the Universe expanded from a single point. In Friedmann's models, the expansion of the Universe is slowed by the gravitational force of matter within the Universe. If the density of matter (Ω) in the Universe exceeded a critical amount, it would be sufficient enough to stop expansion and cause the Universe to fall back in on itself; this is called a "closed" Universe. If the amount of material in the Universe was less than the critical amount the Universe would continue to expand forever, called an "open" Universe. In the case where the amount of matter matches the critical amount, the rate of expansion would fall to zero after infinite time. The currently accepted model of the Universe extends Friedmann's model to include a "dark energy" contribution like Einstein's cosmological constant.

1.2   Expansion of the Universe

In the late 1920s observations of galaxies using optical spectroscopy had allowed the calculation of their velocities as compared to Earth. These measurements were combined with their distances, as determined using standard candles like Cepheid variable stars, to create a plot of speed versus distance. Aside from our closest galactic neighbors, it was shown that the further away a galaxy was the faster its rate of recession. Hubble's Law was derived from this relation in which the speed of recession and distance are directly proportional and are related by Hubble's constant (H_o) (Hubble, 1929). This type of linear relationship is a consequence of observing a Universe that is uniformly expanding. If you assume the Universe has expanded at this uniform rate throughout its existence, then it is possible to rewind time and discover a moment when the Universe would have had no size.

When a photon travels through space its properties change due to this expansion. In particular, when a photon is emitted (with wavelength λ_{rest}) it will undergo an elongation of its wavelength as it travels through space. This elongation is due to the expansion of the Universe while the photon is traveling. The amount of expansion that has occurred in the Universe while

the photon has been traveling is exactly the same ratio in which the photon wavelength will been elongated. When the photon reaches us we observe it with wavelength $\lambda_{observed}$. This elongation of the wavelength is called, "cosmological redshift". It is possible to characterize the recession (redshift) or approach (blueshift) of a galaxy by the relative difference between the observed wavelength that we see on Earth, here and now, and the wavelength that was emitted from an object (there will be a difference due to the expansion of space). This is given by the dimensionless quantity z

$$z = \frac{\lambda_{observed} - \lambda_{rest}}{\lambda_{observed}}. \tag{1.1}$$

1.3   The Cosmic Microwave Background

Gamow (Gamow, 1948) was the first to predict the earlier Universe should have left radiation that could still be detected today. This radiation was initially in the form of high energy gamma rays and became less energetic as the Universe expanded and cooled. Up to the first 380,000 years after the beginning of the Universe the photon energy was high enough to prevent any formation of light atoms in the Universe and therefore it was composed of hydrogen and helium nuclei and free electrons; it was a plasma. These free electrons scattered the photons before they could travel far and thus the Universe was opaque. As the Universe cooled, the photons became decoupled and could free-stream through space unimpeded. This coupling between matter and radiation in the early Universe has two important observable ramifications: first, the radiation should have a black body spectrum (spectrum of a heated, opaque object) which corresponds to the temperature of the Universe right before the photons could travel free (approximately 380,000 years after the start): and secondly, the distribution of the nuclei and electrons (baryonic matter) would have been related. This radiation remaining from the Big Bang is known as the cosmic microwave background (CMB). It is called "microwave" because the wavelengths (of maximum intensity) have been stretched into to the microwave-wavelength range. This was proved observationally in 1965 (Penzias & Wilson, 1965). However, incontrovertible proof as to its origin came in 1992 when the Cosmic Background Explorer (COBE) satellite showed the

background radiation had the precise black body spectrum that was hypothesized (Smoot et al., 1992). COBE's measurements verified the CMB had the precise spectrum that would result from a Big Bang scenario.

1.4   Inflation

Given the Big Bang's observational success, there were still some problems with the theory. One is that the Universe appears to have exactly the same temperature in opposing directions. In a standard Big Bang model with uniform expansion there hasn't been enough time to allow radiation to travel from one region of the sky to the other. The consequence is these regions cannot exchange their properties with one another to become exactly the same; energy cannot travel faster than the speed of light. Secondly, observations show the Universe is very close to being flat, $\Omega \sim 1$, and the Big Bang theory gives no particular reason why this should be the case.

This issue was reconciled with an idea of "inflation", first proposed by Alan Guth (Guth, 1981). In his theory, the volume of space expanded exponentially. Before this, the volume of space was small enough that radiation could travel across and give it a uniform temperature. Inflation also ensures the exponential expansion of space would force the geometry of space to become flat.

1.5   Dark Matter and its Evidence

Inflation predicts that space has zero curvature (flat) and the required mass-energy for this to be true is larger than the mass-energy apparently available in baryonic matter. This provided motivation for the presence of non-baryonic dark matter (DM), matter not detectable by electromagnetic radiation, hence "dark". Observational evidence supporting the presence of non-baryonic dark matter is discussed below.

1.5.1   Big Bang Nucleosynthesis

The density of baryonic matter in the Universe is highly constrained by nucleosynthesis in the early Universe. A few minutes after the Big Bang, one would expect conditions in the Universe to allow nucleosynthesis (the fusion of protons to elements with larger nuclei, coined Big Bang nucleosynthesis (BBN)). The light elements created this way are very sensitive to the baryon-photon ratio. These elements can be detected in regions where no star formation has occurred and therefore the region is close to primordial composition. Observations of H, He, Li and their isotopes in these regions provide a measurement of the baryon-photon ratio in the early Universe and put an upper limit on baryonic matter at about 4% (Gamow, 1948).

1.5.2   Galactic Rotation Curves

The observed rotation velocities of baryonic matter (stars and gas) are measured as a function of their distance from the center of rotation of a galaxy. Kepler's law gives

$$V_r = \sqrt{\frac{GM_r}{r}}, \tag{1.2}$$

which gives velocity as a function of the gravitating mass M_r at each radius r (see Fig 1.1). If most of the mass in galaxies was luminous, one would expect V_r to decrease as one moved out into the lower-luminosity parts of the outer disk. However, V_r is observed to stay constant regardless of distance (Fig 1.2). These studies reveal (a) the DM considerably exceeds the amount of visible baryonic mass, and (b) the invisible DM, responsible for the rotation velocities, is distributed in a much larger halo than the luminous baryonic matter (Sofue & Rubin, 2001).

1.5.3   X-ray Gas of Galaxy Clusters

Clusters of galaxies are filled with extremely hot gas that is 10^7-10^8 K. At this temperature the kinetic energy of the gas particles are too great to be bound by the mass of the baryonic matter within the cluster. For these gas particles to remain in the vicinity of the cluster the total mass of the system has to be many times the known luminous mass (Voit, 2005).
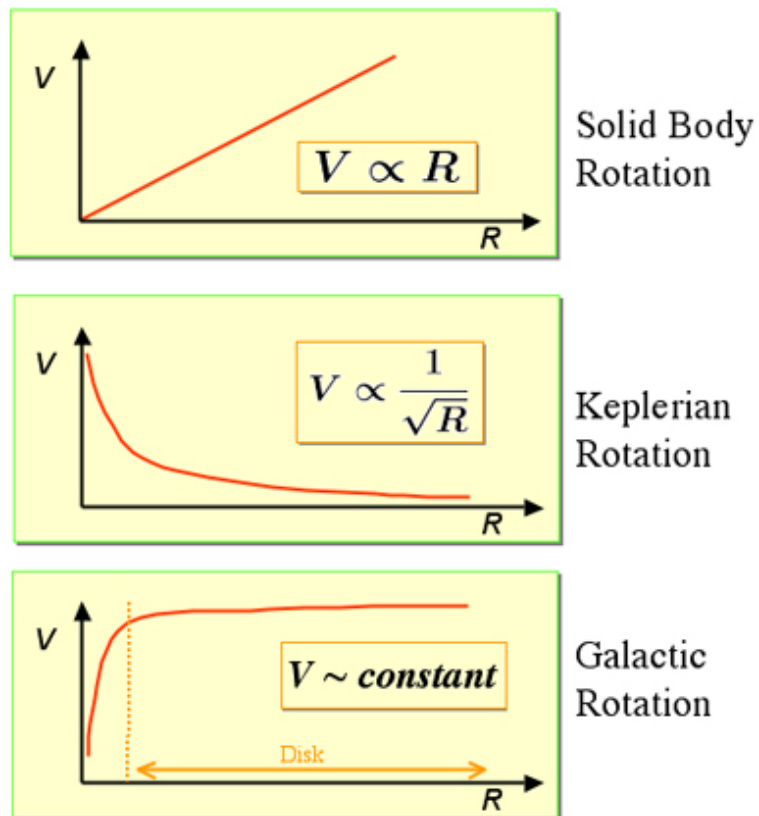
Figure 1.1: Figure taken from https://astronomy.swin.edu.au/cosmos/R/Rotation+Curve. A rotation curve is a plot showing how orbital velocity, V, varies with distance from the centre of the object, R. Rotation curves can be determined for any rotating object. They are generally used to show how mass is distributed in the Solar System (Keplerian Rotation curves) or in spiral galaxies (galactic rotation curves).
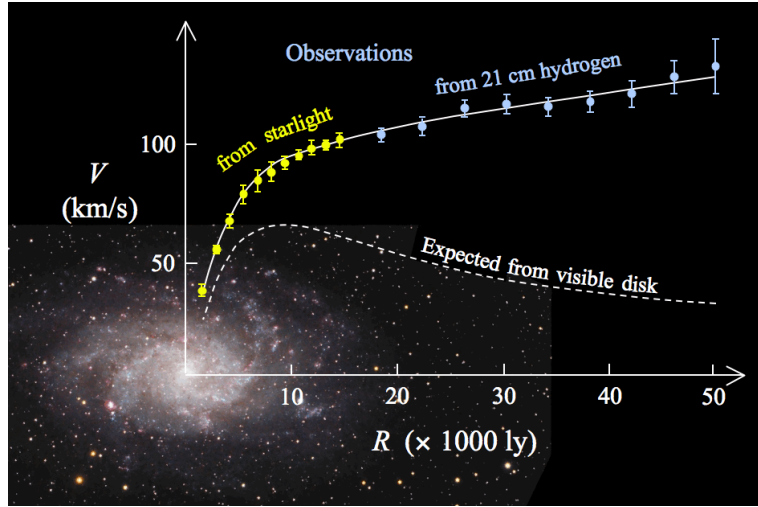
Figure 1.2: Figure taken from http://www.arturostabile.com/publications.html. A diagram showing the expected rotation curve for a galaxy and the actual rotation curve from observational data.

1.5.4 Gravitational Lensing

Predictions from Einstein's General Theory of Relativity (Einstein, 1916) states that mass distorts the geometry of spacetime, causing even light to "bend" near a massive object. Therefore, the mass of a cluster of a galaxies can distort the photon paths of more distant objects. The light rays coming to us from a distant object along a path which passes near some foreground massive object of mass M are expected to be deflected slightly by the latter, by an angle

$$\alpha = \frac{4GM}{c^2 b} \equiv \frac{2R_S}{b},$$

(1.3)

where b is the "impact parameter" (the minimum distance of approach of the light ray to the mass M) and $R_S = \frac{2GM}{c^2}$ is the Schwarzschild radius. This leads to a distortion in the shapes of background galaxies. The total mass of the foreground cluster can be estimated from the amount of distortion of the background galaxies. The total mass of galaxy clusters detected this way show there is vastly more mass than the luminous mass seen in stars and gas and thus provides strong evidence for the existence of dark matter.

7

1.6 Dark Energy

In the 1990's observations of another type of standard candle, Type 1a supernovae, allowed for testing of the Hubble expansion relation. These objects, which are much further away than previous standard candles, like Cepheid variable stars, allowed the Hubble plot, relating distance and speed, to be extended. Given a specific distance one could predict the speed at which the object should be receding. Contrary to the accepted belief, it was found that these objects were receding faster than predicted. This implies that the expansion rate of the Universe is increasing - not decreasing (as expected) - and thus evidence for an additional component of the energy-density in the Universe, often called dark-energy, with a similiar effect as Einstein's Λ (Riess et al., 1998) (Fig 1.3).

A positive Λ term in Einstein's cosmological equations can be described as a fixed positive energy density. This positive energy-density exists within the fabric of space and is unchanging with time. This is often called the "cosmological constant" and successfully explains a variety of observations. It has become an accepted constant in the current standard model of cosmology, the lambda-cold dark matter model (ΛCDM), which incorporates both cold dark matter (Section 1.8) and the cosmological constant.

The amount of baryonic matter makes up $\sim 4\%$ of the total mass-energy content and dark matter makes up $\sim 23\%$ of the total mass-energy content of the Universe. Thus, some 73%, is thought to be a form of energy that is uniform throughout space (Perlmutter et al., 1999).

The density in different components is usually expressed in terms of the critical density (the density required to make the Universe spatially flat) ie. $\Omega_{matter} = \rho_{matter}/\rho_{critical}$, and $\Omega_{\Lambda} = \rho_{\Lambda}/\rho_{critical}$. In the standard model $\Omega_{total} = \Omega_{matter} + \Omega_{\Lambda} = 1$, ie the Universe is spatially flat.

1.7 The Evolution of Structure

The Universe contains regions of denser mass-energy content (stars, galaxies, clusters of galaxies, etc), which evolve and become increasingly more compact and complex as time goes on. It is thought that these density inhomogeneities originated from small perturbations (from quantum

8
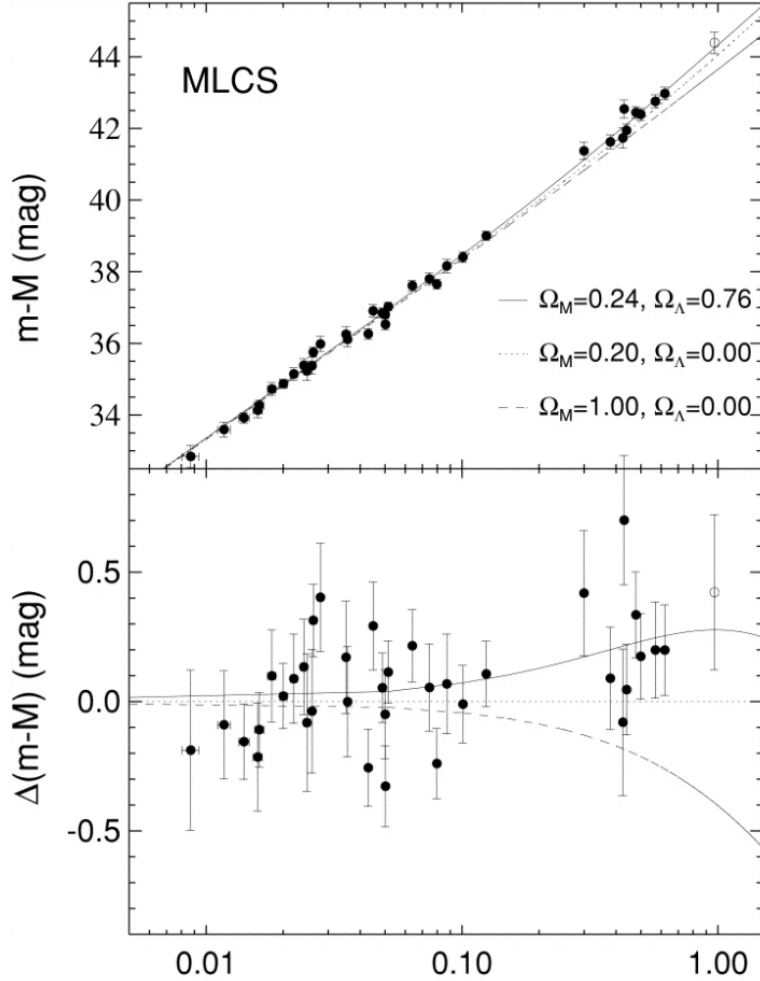
Figure 1.3: Figure taken from Riess et al. (1998). Multicolor Light Curve Survey (MLCS) SNe Ia Hubble diagram. The upper panel shows the Hubble diagram for the low-redshift and high-redshift SNe Ia samples with distances measured from the MLCS method. Overplotted are three cosmologies: "low" and "high" Ω_M with $\Omega_\Lambda = 0$ and the best fit for a flat cosmology, $\Omega_M = 0.24$, $\Omega_\Lambda = 0.76$. The bottom panel shows the difference between data and models with $\Omega_M = 0.20$, $\Omega_\Lambda = 0$. The open symbol is SN 1997ck (z = 0.97), which lacks spectroscopic classification and a color measurement. The average difference between the data and the $\Omega_M = 0.20$, $\Omega_\Lambda = 0$ prediction is 0.25 mag.

fluctuations), where the density is slightly above average: $\rho = \rho_{average} + \rho_\Delta$, where $\rho_{average}$ is the average density and ρ_Δ is the density excess; ρ_Δ is much smaller than the average (to start). Under the action of gravity these small density excesses grow larger, until eventually the excesses become significant compared to the average density, $\rho_\Delta > \rho_{average}$, described by saying that the excesses have become "non-linear". The process involves a hierarchy of semi-chaotic sub-structures existing in a continuum of mass scales. These excess-density, or over-dense, regions arrange themselves under the action of gravity into ever larger regions (Peebles, 1980).

1.7.1 Evolution of Dark Matter Halos

Dark matter, being collision-less, passes through itself and re-expands until it reaches its approximate virial equilibrium configuration. Within the ΛCDM scenario outlined above, large scale structures in the Universe such as galaxies and clusters of galaxies form hierarchically. Small DM halos tend to occur inside an underlying larger scale over-density region, which gives the small DM halo an extra boost, a "biasing" in the formation process. In the course of time the smaller DM halos are expected to merge, before or after stars formed in them, giving rise to larger DM halos and larger galaxies. Even later, the underlying larger scale over-density regions themselves would become "non-linear", giving rise to a distinct cluster of galaxies.

1.7.2 Evolution of the Baryonic Matter

As the various mass scales collapse the baryons represent a minor constituent that falls into the potential wells provided by the associated dark matter. The baryonic gas is dominated by the gravitational field of the DM. Thus, the baryons initially follow the DM during the early phases of the collapse. As the collapse proceeds, the volume occupied by the DM and the gas decreases and both are adiabatically heated. However, unlike the DM, the baryonic gas has a significant "cross-section" for interacting and can't pass through itself. This gives rise to a further heating caused by collisions. The increased motions of the gas (higher temperature) excite their electrons to higher quantum energy levels which are followed by radiative de-excitation. Therefore, the photons carry away much of the acquired thermal energy of the gas, and cools the gas, allowing

it to settle into more compact configurations than the parent dark matter halo in which it nests.

1.8 Predicting Large-Scale Structure

The full details of the growth of structure are complicated and only approximately understood. For example, it is possible to calculate how density fluctuations will evolve when they are in the linear regime but to understand non-linear evolution large simulations are required.

To understand these processes we use observational and theoretical techniques. We can measure the constants of cosmology such as: Hubble's constant (H_0), Ω_{matter} and Ω_{Λ}. The values of these constants determine how rapidly the Universe expanded. The more rapidly the Universe is expanding the more difficult it is for gravity to pull material together into galaxies and larger-scale structures.

The available observations and measured constants of cosmology become inputs to theoretical models and supercomputer simulations. The simulations model the formation and evolution of dark matter halos, small and large galaxies, and galaxy groups and clusters. The simulations seek to approximate what the Universe should look like at different times (different redshifts) and can then be compared to the observations. The abundance and distribution of large scale structure can provide strong constraints on cosmological parameters (Bahcall & Fan, 1998) and (Viana & Liddle, 1999).

1.9 Detecting Galaxy Clusters

Simulations have shown that the number counts of galaxy clusters, among other things, is sensitive to cosmological parameters (Haiman et al., 2001). Simulations also predict specific masses for galaxy clusters at different times in the Universe. To be able to test these predictions and constrain measurements of the cosmological constants, it is required that we know the mass and redshift distributions of clusters with good precision. To do that we need to find galaxy clusters and measure their masses. This can be done by exploiting some of the properties of galaxy clusters discussed earlier in proving dark matter's existence.

11

1.9.1 X-ray Observations

As we have seen in Section 1.5.3, galaxy clusters contain extremely hot gas. An optically thin, hot gas primarily emits spectral lines. However, if the gas is a plasma, with its temperature on the order of millions of degrees, then all the atoms are broken up and the radiation is produced only when charged particles in the plasma are decelerated due to mutual Coulomb interactions amongst themselves. Such radiation, called bremsstrahlung or free-free radiation, is emitted. This type of radiation can be detected in the X-ray part of the spectrum. There are multiple space-based instruments (XMM-Newton, Chandra, ROSAT, etc.) conducting surveys (REXCESS, All-Sky-Surveys, etc.) to detect such phenomenon (Polletta et al., 2007; Romer et al., 2001; Sahlén et al., 2009). In the case of a galaxy cluster, X-ray luminosity is related to the temperature of the gas and can be used to infer how much mass is present in the system. Alternatively, the temperature of the gas can be estimated directly using the features in the X-ray spectra.

1.9.2 Optical Observations

Optical surveys, such as the Sloan Digital Sky Survey (SDSS), can also be used to detect galaxy clusters (Popesso et al., 2005; Yang et al., 2008). Optical surveys map large portions of the sky to obtain positional information (RA, Dec, and z) of astronomical objects. There are different ways to locate galaxy clusters in optical surveys. One example is red-sequence studies (Zehavi et al., 2011), which evaluate if there is a certain density of red objects within a given radius. By collecting dynamical information on the galaxies within a cluster you can determine mass from the virial theorem (discussed below). Observations indicate clusters are gravitationally bound (Sofue & Rubin, 2001). Peculiar velocities of galaxies within a cluster can be determined via

$$\Delta v_i = c \frac{(z_i - \bar{z})}{(1 + \bar{z})},\tag{1.4}$$

where Δv_i is the peculiar velocity of the ith galaxy, z_i is its redshift, and $\bar{z}$ is the redshift of the cluster. If the peculiar velocities are found, it is possible to estimate the total mass of the cluster from the virial mass, given by the equation

$$M = \left(\frac{5}{3}\right) \frac{<v^2> R}{G}, \tag{1.5}$$

where G is the gravitational constant, v is velocity, and R is the given radius.

1.9.3 Microwave Observations

Observations of the CMB can also reveal large scale structure. The COBE spacecraft observations showed the CMB did not have a perfectly uniform temperature and, since then, observations from Wilkinson Microwave Anisotropy Probe (WMAP) and Plank spacecraft, etc. have been able to map these inhomogeneities in the CMB temperature (fluctuations in the observed temperature of typically $60\,\mu$K).

Temperature anisotropies trace density fluctuations in the early Universe. This effect is caused by the radiation wavelength being stretched by the gravitational potential well created from the DM. This is called, "gravitational redshift". The photons leaving from areas that were DM dominated would have longer wavelengths than photons leaving areas with less dark matter. Since the spectra from these two regions differ, the black body temperature from these regions differ, explaining the temperature differences that are observed. Observations of the CMB provide a direct probe of density fluctuations in the early Universe but they can also be used to detect clusters of galaxies at lower redshifts, via the Sunyaev-Zel'dovich-effect described in Chapter 3 ie. CMB observations can also be used to probe large scale structure at low redshift.

1.10 Tracing Cosmic Evolution

Studies of clusters of galaxies have had a wide impact on our understanding of galaxy formation and cosmology (Voit, 2005). The number counts of clusters and their distribution in redshift is sensitive to cosmological parameters: the variance in density in eight Mpc spheres ($\sigma8$), the mass-energy density in baryons (Section 1.5.1), dark matter and dark energy (Section 1.5, 1.6), and the equation of state of the latter. (Bahcall & Fan, 1998; Evrard et al., 2008; Mantz et al.,

2010; Rozo et al., 2010; Vikhlinin et al., 2009). Studying cluster counts as a function of redshift is thus a useful probe of cosmological parameters.

The Sunyaev-Zel'dovich Effect

2.1 Introduction to the Sunyaev-Zel'dovich Effect

As we have seen in Section 1.3, the CMB radiation appears isotropic. However, observations reveal small anisotropies in the CMB. Some of these anisotropies have primordial origin but others are due to secondary effects. The secondary effects are produced by structure along the line of sight to the CMB. One source of anisotropy is the the Sunyaev-Zel'dovich effect which has to do with the interaction between the CMB photons and the clusters of galaxies it passes through. The interaction is with the hot, low density intracluster gas. The background radiation interacts with the electrons in the gas via inverse Compton scattering. In Compton scattering, the photon initially has more energy than the electron, some energy is transferred from the photon to the electron. Since the photon loses energy, the wavelength increases (energy decreases). However, it is also possible for the electron to start out with more energy than the photon. In this case, called inverse Compton scattering, energy is transferred from the electron to the photon. The wavelength of the photon decreases (energy increases). The electrons in the intracluster gas have high energies, and low-energy photons get a large boost in energy, going in as radio wavelength

15
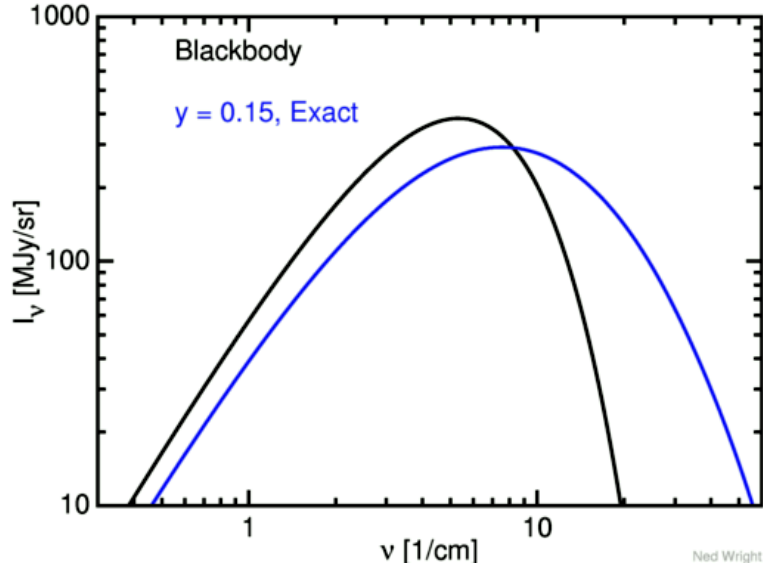
Figure 2.1: Figure from Ned Wright (www.astro.ucla.edu/ wright/SZ-spectrum.html). The black-body (black line) and distorted spectrum (blue line) on a log-log scale showing the Sunyaev-Zel'dovich-effect

photons and coming out at shorter wavelengths. This means that if we look in the directions of clusters of galaxies at microwave wavelengths, some of the background CMB radiation will have been removed since some of the radio photons have been shifted to higher energy. This is called the thermal Sunyaev-Zel'dovich effect (Fig 2.1).

More quantitatively, when the temperature of the electrons are much greater than the Compton temperature, there is a net transfer of energy from electrons to photons, by a factor of

$$1 + \frac{4kT}{m_e c^2}, \tag{2.1}$$

where the magnitude of this effect is proportional to the Compton parameter, y, a measure of the gas pressure integrated along the line-of-sight

$$y = \frac{\sigma_T}{m_e c^2} \int P \mathrm{d}l, \tag{2.2}$$

where σ_T is the Thomson cross-section, c the speed of light, m_e the electron rest mass, and $P = n_e T$ is the product of the electron number density and temperature. The total SZE signal,

integrated over the cluster extent, is proportional to the integrated Compton parameter Y_{SZ} where

$$Y_{SZ} D_A^2 = (\frac{\sigma T}{m_e c^2}) \int P \mathrm{d}V, \tag{2.3}$$

where D_A is the angular distance to the system.

2.2 The SZE-Mass Relations

The SZE surface brightness, in principle, is independent of the redshift. SZE surveys operate on a different observed effect, resulting in a different selection function of clusters, resulting in different redshift and mass ranges than X-ray and optical cluster surveys do. SZE surveys are generally more sensitive to higher redshift and more massive clusters. The combination of these characteristics make it more robust, being able to put tight constraints on cosmological parameters (Battaglia et al., 2012) (this makes it an ideal probe for mass evolution). Within the last few years, blind identification of clusters has begun. The identification of massive, rare clusters enables us to probe the current cosmological parameters. To do this we need to accurately determine the mass of these clusters. Direct measurement of mass would be ideal, but mostly, mass is inferred indirectly from optical, X-ray, and microwave observations; each method having its own complications. A thermal Sunyaev-Zel'dovich measurement directly observes the cluster's total gas heat-energy content, a volume average of the thermal gas pressure, and therefore its gravitational energy through the virial relation (Section 1.5), so it is expected to provide a robust probe of cluster mass.

A handful of recent studies have attempted to correlate the SZE with other cluster observables in order to determine a precise relationship between the two observables and apply the correlation to other clusters. Below, I summarize some of these studies.

2.2.1 X-ray Pressure Profiles and the SZE-Mass Relation

Arnaud et al. (2010) studies the pressure profiles of nearby cluster systems. Their study is based on the concept that the gas pressure of the system is directly linked to the gravitational potential

well and therefore the mass of the system. This is supported by the work of numerical simulations (Bonaldi et al., 2007) and analytical models (Reid & Spergel, 2006). The numerical and analytical simulations show that the dynamical state of the cluster and gas introduce little scatter into the Y_{SZ} - M relation. However, they do point out the normalization of the relation and the amount of intrinsic scatter does depend on the gas physics (Bonaldi et al., 2007; Vikhlinin et al., 2006). It is the goal of Arnaud et al. (2010) to understand the pressure profiles that give rise to this relation and calibrate these quantities with observational data.

Arnaud et al. (2010) sets out to derive pressure profiles based on an X-ray analogue of the integrated Compton parameter, Y_X. This is an important physical parameter as it is the product of M_{500} and the spectroscopic temperature outside the core, T_X. However, this relation does depend on cluster structure

$$\frac{Y_{SZ}D_A^2}{Y_X} = \frac{\sigma_T}{m_e c^2} \frac{1}{\mu_e m_p} \frac{<n_e T>}{<n_e>_{R_{500}} T_X},$$
(2.4)

where $Y_{SZ}D_A^2$ is the SZE integrated over a given area, Y_X is defined as the product of M_{500}, the gas mass within R_{500} and T_X, the spectroscopic temperature outside the core. R_{500} is the radius at which the mean density is 500 times the critical density of the Universe. M_{500} is the amount of mass inside R_{500}. σ_T is the Compton-temperature, m_e is the electron mass, m_p is the proton mass, n_e is the number of electrons, T_X is the X-ray luminosity, and the angle brackets represent volume averaged quantities.

By understanding the radial pressure distribution they can probe the intra-cluster gas properties of the system. Arnaud et al's analysis is done by studying cluster pressure profiles of 33 local ($z < 0.2$) clusters drawn from the REXCESS catalog and observed with $XMM - Newton$. Arnaud et al (Arnaud et al., 2010) combined observational data and simulation data to derive a universal pressure profile (UPP). The combined data is generated from their simulations, independent simulations, observed data from this study, and archival data of clusters in a similar thermodynamical state. This approach gives robustness to their UPP. Their UPP provides SZE decrement information and relations for the Compton parameter in various apertures. They show that varying the profile shapes do not introduce extra scatter into the Y_{500} - M_{500} relation (unlike

the Y_X - M_{500}). Their derived relation

$$h(z)^{-2/3}Y_{SZ,R500} = 10^{-4.739} \times \left[\frac{M_{500}}{3 \times 10^{14}h_{70}^{-1}M_\odot}\right]^{1.79} h_{70}^{-5/2}\text{Mpc}^2. \tag{2.5}$$

Arnaud et al. (2010) states they were not able to explore pressure evolution with their given cluster sample. Since their data was composed solely of local clusters they had to assume standard self-similar evolution. They express optimism in the ability of Atacama Cosmology Telescope (ACT) and the South Pole Telescope (SPT) surveys to detect massive, high z, clusters, allowing the study of the evolution of pressure profiles and to probe the evolution of the Y_{SZ} - M_{500} relation.

2.2.2 Gravitational Lensing and the SZE-Mass Relation

Marrone et al. (2012) present the first weak-lensing based scaling relation between galaxy cluster mass, M_{WL} , and integrated Compton parameter Y_{SZ}. Weak lensing probes the gravitational potential of the cluster without using gas-physics, providing a way to test for mass biases in other mass estimators. Marrone et al. (2012) observed 18 galaxy clusters at $z = 0.2$ with the Subaru 8.2 m telescope and the Sunyaev-Zel'dovich Array. These clusters were selected from the Local Cluster Substructure Survey (LoCuSS), a multi-wavelength survey of galaxy clusters selected from the ROSAT All-Sky Survey (Okabe et al., 2010). The clusters were drawn from the LoCuSS "high-L_x" sample which were selected from the ROSAT survey.

The weak-lensing measurements are based on data from the Subaru/Suprime-Cam23. They selected weakly-lensed background galaxies based on a minimum color offset from the cluster red-sequence. The background galaxy shapes were measured in accordance with the KSB method (Kaiser et al., 1995) and the number density of galaxies used in the analysis was $\backsim$10-30 per arcmin^2. Their derived relation is

$$\frac{M(r_\Delta)}{10^{14}M_\odot} = 10^A \times \left[\frac{Y_{SZ}D_A^2E(z)^{-2/3}}{10^{-5}\text{Mpc}^2}\right]^B, \tag{2.6}$$

where B is 0.44 and A is 0.367 assuming a flat λ-CDM cosmology: $\Omega_M = 0.27$, $\Omega_\Delta = 0.73$, and $H_0 = 73$ km s^{-1} Mpc^{-1}.

They examine their derived Y-M_{WL} relation and its scatter, along with the possibility of biases in the mass estimates relating to cluster morphology. Marrone et al. (2012) reports their scaling relations are subject to some bias because of the L_x selection method of the "high-L_X" sample. Their results are consistent to within 1σ of (Bonamente et al., 2008) at R_{2500} but are less consistent with Andersson et al. (2011) values at R_{500}.

In their Y_{sph}-M_{WL} relations they indicate large intrinsic scatter that may be related to cluster morphology. They detect a significant difference in the normalization of the self-similar Y_{sph}-M_{WL} relations between disturbed and undisturbed clusters (which they determine by measuring a centroid shift of the X-ray peak compared to the centroid of emission) at all three overdensity radii they study. However, this systematic effect has not been seen in simulations. It has been found that the SZE signal is a robust mass proxy even during periods of mass accretion (Motl et al., 2005). The scatter in Marrone et al's signal is larger than predicted in simulations of the SZE signal, although this is not unanticipated. They reason most of the scatter comes from calculating spherical masses from the intrinsically two-dimensional measurements. Much of the segregation they see between disturbed and undisturbed clusters is explained by modeling spheroidal halos as spheres when determining masses. This explanation is supported by showing the similarity between their measurements and predictions of projection-induced scatter for weak-lensing data of similar quality. I compare their Y_{sph}-M_{WL} derived relation to our data in Section 4.2.

2.2.3   Dynamical Measurements and SZE-Mass Relations

The most used method for determining cluster mass comes from optical spectroscopy. These observations allow for velocity dispersions of the cluster to be measured and therefore mass. This method doesn't require one to observe from space and is another way to measure the mass variable independently of the gas properties. The fundamental underlying assumption is that the galaxy cluster is virialized; it is not undergoing merging.

Sifón et al. (2012) presents the first dynamical mass estimates and $Y_{SZ} - M$ scaling relations for a sample of SZE selected galaxy clusters. Their sample consists of 16 clusters detected with

the ACT in a 455 deg^2 area of the southern sky. These clusters were observed by ACT in its 2008 southern sky survey at 148 GHz (Marriage et al., 2011), and were optically confirmed by (Menanteau et al., 2010). The spectroscopic redshift range covered by the sample is $0.28 < z < 1.07$ with a median redshift $z = 0.50$. On average, 60 galaxies were used in the analysis of each cluster.

The spectroscopic observations were carried out at VLT and Gemini South in Chile. They selected their targets by constructing a photometric redshift-selected catalog and included galaxies within ± 0.1 of the redshift of the BCG. Galaxies within this subset were then visually selected based on their $g, r,$ and i colors, with preference given to bright galaxies. All their spectroscopic observations cover the wavelength range $\backsim$ 4000 - 8000 Å. In this range several spectral features are observable at the median photometric redshift of 0.54 (Menanteau et al., 2010). These are mainly the CaII K-H absorption doublet (at a rest-frame wavelength $\lambda_0 \backsim 3950$ Å), which is the spectral signature of elliptical galaxies, plus other absorption lines.

In this work, they restricted themselves to a power-law relation between dynamical mass and each SZE estimator measured from the ACT data. We are most concerned with the M$_{200}$ estimator of the form

$$\frac{M_{200c}}{h_{70}^{-1}M_\odot} = 10^A \left[\frac{Y_{200c}D_A(z)^2 E(z)^{-2/3}}{5 \times 10^{-5}h_{70}^{-2}\text{Mpc}^2} \right]^B . \tag{2.7}$$

Here, $D_A(z)$ is the angular diameter distance in Mpc, M_{200c} is in units of $h_{70}^{-1}M_\odot$, $E(z) = [\Omega_M(1+z)^3 + \Omega_\Lambda]^{1/2}$, and A and B are the fit parameters for the slope and the normalization, respectively. They use the Bivariate Correlated Errors and intrinsic Scatter (BCES) algorithm for the linear regression (Akritas & Bershady, 1996). This method accounts for correlated measurement errors in both variables. We compare our results to this relation in Section 4.2.

From the available 3-d information they divided the sample into relaxed and disturbed clusters. There were three different tests to see if a cluster was determined as relaxed or disturbed. The factors considered were the peculiar BCG velocity, the projected BCG-SZE offset, and the Dressler & Shectman substructure test (Dressler & Shectman, 1988). Clusters were determined as merging if they met at least two of these conditions (a more quantitative explanation of each

test is available in Sifón et al. (2012)). Sifón et al. (2012) find that ∽50% of the clusters are disturbed. Given the large number of disturbed clusters, they call for further studies to assess the morphological impact on their relation. Regardless, they report their scatter is within that of other self-similar evolution simulations of clusters and their scaling relation is in good agreement with previous results.

2.2.4 Simulations of SZE Relations

The use of SZE surveys for determining cosmological parameters from cluster abundances is limited by the theoretical uncertainties in the $Y - M$ relation. Battaglia et al. (2012) investigate how non-thermal pressure and irregular shapes of the gas distribution of the intra cluster medium (ICM) effects $Y - M$ scaling. They aim to identify other observable parameters that would mimic internal gas flows in effort to reduce Y-M scatter. Battaglia et al's study investigates the influence of various physical effects on the Y-M scaling relation. Characterization of these effects would allow for tighter constraints on cosmological parameters. This is done with hydrodynamic simulations of the cosmic web.

They investigate the effects of varying radiative cooling, supernova feedback, star formation, AGN, cosmic rays, and other entropy injection and transport mechanisms. Using the Y_Δ values they calculated from modeling various systems, they fit an average scaling relation

$$Y_\Delta = 10^B \left[\frac{M_\Delta}{3 \times 10^{14} h_{70}^{-1} M_\odot} \right]^A h_{70}^{-1} \text{Mpc}^2, \qquad (2.8)$$

where A and B are the fit parameters for the slope and the normalization, respectively. They weight each cluster by its Y_Δ value when fitting for A and B to keep the low-mass clusters from dominating the fit. They note this could lead to potential biasing of parameters since Y_Δ is the dependent variable in the $Y - M$ relation. They test for this by weighting each cluster by $M_\Delta^{5/3}$, the scaled independent variable and only found negligible difference between the weighting schemes for amplitude and slope. We compare our results to the Battaglia et al. (2012) relation in Section 4.2.

SALT Observations of ACT SZ Clusters

Sehgal et al. (2011) and others have shown that without an accurate calibration of the scaling relation between cluster mass and SZE signal, the 2008 ACT southern cluster sample is unable to constrain cosmological parameters to much better precision than the WMAP7 CMB data alone. However, with a well characterised Y-M relation (i.e., the aim of this project to aid in that goal), the ACT+WMAP7 constraints will be significantly improved, assuming cluster mass errors of 25%. As we have seen with Sifón et al. (2012), dynamical mass estimates from SZE-selected clusters from ACT have produced results instrumental for a well-characterised Y-M relation. Their results show that masses determined from dynamical measurements provide a sound method for relating the SZE to cluster masses. This method, in combination with other mass proxies, will tighten constraints on cosmological parameters. In Hasselfield et al. (2013), they find that including dynamical mass data for only seven clusters in the cosmological analysis resulted in a significant improvement in the measurement of cosmological parameters.

We present Southern African Large Telescope follow-up observations of seven massive clusters detected by the Atacama Cosmology Telescope using the Sunyaev-Zel'dovich effect. We conducted multi-object spectroscopic (MOS) observations with the Robert Stobie Spectrograph

(RSS) in order to measure galaxy redshifts in each cluster field, determine the cluster line of sight velocity dispersions, and infer the cluster dynamical masses. We have supplemented our data with redshifts from the Sloan Digital Sky Survey (SDSS) archival data with approximately 20 percent of our identified cluster members coming from SDSS.

3.1   ACT Maps and Cluster Detection

The ACT maps and cluster identification are provided by the ACT team. The Atacama Cosmology Telescope is a six-metre telescope on Cerro Toco in the Atacama Desert. It resides at an altitude of 5200 m and is designed to make high-resolution microwave-wavelength surveys to study the CMB. Observations are made in three different frequencies: 148 GHz, 218GHz, and 277 GHz. Each frequency is measured by a total of 1024 transition-edge sensors which allow measurements of the CMB to within a few millionths of a degree (Fowler et al., 2007). In 2009 and 2010, ACT observed the celestial equator. The region observed overlaps 270 square degrees with SDSS, including SDSS's deep (r ∿24) Stripe 82 region. This region is the lowest noise area in the ACT equatorial maps. The ACT team has identified and optically confirmed 69 clusters from S82 with S/N > 4 ((Menanteau et al., 2013), (Hasselfield et al., 2013)), spanning the redshift range $0.2 < z < 1.4$, with a median $z = 0.5$.

3.2   SALT Observations

Observations of seven ACT clusters were conducted with the RSS in multi-object spectroscopy (MOS) mode, which uses custom designed slit masks. The slit masks and SALT Phase 1 and 2 proposals were designed and written by Dr Matthew Hilton and Susan Wilson. Given that SALT is located at Sutherland where the median seeing is 1.3' (Catala et al., 2013), slitlets with dimensions of 1.5' width and 10' length were used. This was chosen to ensure reasonably accurate sky subtraction given the seeing conditions. The RSS has an 8' diameter circular field of view, and with these slit dimensions, able to target 19-26 galaxies in each cluster field per slit mask. Three to four bright ($15 - 17.5$ magnitude in the *r* band) stars per cluster were chosen in

the field for alignment of the slit masks during acquisition.

The slit masks were designed in regards to the catalogs extracted from the 7th data release of the Sloan Digital Sky Survey (Abazajian et al., 2009). For each cluster, the Brightest Cluster Galaxy was identified from visual inspection of the SDSS images, and the color of the red-sequence was identified from visual inspection of color-magnitude diagrams. This information was used to define target galaxy samples for each cluster, prioritizing the selection of galaxies with magnitudes fainter than the BCG and with color bluer than the estimate of the red-edge of the red-sequence (note that these color - magnitude cuts vary from cluster-to-cluster due to their slightly different redshifts). Target galaxies were assigned slits in an automated fashion using an algorithm that prioritized objects closer to the cluster center (in practice, this ensured that the number of objects whose spectra were centered horizontally on the detector array was maximized). The final masks were made using the PYSLITMASK tool, part of the PYSALT software package (Crawford et al., 2010). Three masks per target were designed, although not all masks were observed.

The SALT observations were carried out by the on-duty SALT astronomer on the given night of observation. These RSS observations were conducted using the pg0900 Volume Phase Holographic (VPH) grating. All observations were conducted with the RSS camera station set to $28.75°$ and the grating angle set to $14.375°$. This set up was chosen to center the wavelength coverage on D4000 at $z \approx 0.3$ (i.e., the approximate redshift of the clusters) and results in dispersion $0.49\,\text{Å}$ with $4000-7000\,\text{Å}$ wavelength coverage. The design of SALT limits observations of objects on the celestial equator to approximately $3200\,\text{sec}$ long intervals (referred to as observing blocks). At the start of each observing block the position of the tracker must be reset and the object re-acquired, incurring significant overheads. The on-duty astronomer obtained $2 \times 975\,\text{sec}$ RSS exposures per observing block for our first observations in July-September 2012. For some subsequent observations, $4 \times 975\,\text{sec}$ exposures were obtained by observing each mask in two observing blocks. Note that SALT is a queue-scheduled telescope and observations were obtained (sometimes of the same mask) on different nights throughout each observing semester. Table 3.1 presents a summary of the observations.

Table 3.1: Observing log of SALT observations

Program	Target	Mask	Number of slits	Frames (sec)	Airmass	Date (UT)
2012-1-RSA_UKSC_RU-001	J2058.8+0123	1	23	2×975	1.8	2012 Jul 16
...	J2058.8+0123	2	22	2×975	1.3	2012 Jul 24
...	J2058.8+0123	3	22	2×975	1.3	2012 Sep 06
2012-2-RSA_UKSC_RU-001	J0320.4+0032	1	25	2×975	1.3	2012 Nov 10
...	J0320.4+0032	2	26	4×975	1.3,1.3	2012 Nov 13, 15
...	J0320.4+0032	3	22	4×975	1.3	2012 Nov 16
...	J0219.9+0129	1	22	4×975	1.3,1.3	2012 Nov 15, 16
2013-1-RSA_RU-001	J0045.2-0152	1	26	4×975	1.2,1.2	2013 Sep 01, 05
...	J0045.2-0152	2	25	2×975	1.2	2013 Sep 25
2013-2-RSA_RU-002	J0156.4-0123	1	25	2×975	1.2	2013 Nov 02
...	J0156.4-0123	3	21	2×975	1.3	2014 Jan 03
...	J0348.6-0028	1	25	2×975	1.2	2013 Nov 03
...	J0348.6-0028	2	23	2×975	2.0	2014 Jan 01
...	J0348.6-0028	3	23	4×975	1.3,1.2	2013 Nov 04, 08
...	J0348.6-0028	4	19	4×975	1.3,1.3	2013 Dec 29, 30
...	J0342.7-0017	1	22	2×975	1.2	2014 Jan 03

3.2.1 PySALT Processing

PYSALT[1]is a suite of PYRAF tools for the reduction and analysis of data obtained from the RSS instrument mounted on SALT. More information on PySALT can be found in (Crawford et al., 2010). The PYSALT tasks consist of: preparing the image headers for the pipeline, applying a CCD amplifier gain and crosstalk correction, bias frame subtraction, cosmic-ray cleaning, flat-field corrections, mosaic image creation from multiple CCD extensions, and extraction of aperture slits based on slit geometry. All the tasks are available to use in PyRAF and the basic data reductions for SALT are done using the SALTRED package. I ran each step of the PySALT pipeline and a step-by-step guide is available in the appendix.

3.2.2 IRAF Processing

After PySALT processing I continued the reduction with IRAF[2]. The IRAF tasks are used to: determine a wavelength dispersion function from a calibration lamp (Xenon or Argon), fit and transform the arc dispersion to the science frames, apply a background subtraction of a constant value determined locally within each slitlet, combine images (where available), and extract one dimensional sums across the apertures. A step-by-step guide is available in the appendix.

3.3 Analysis

3.3.1 Cross correlation for redshifts

After PySALT and IRAF processing were complete I analyzed the data. To determine the redshifts of our galaxies I used another IRAF task called XCSAO, which is located in the RVSAO package (Kurtz & Mink, 1998). This task computes a redshift by using the cross-correlation technique (Tonry and Davis 1979). In brief, the cross-correlation technique assumes that a galaxy spectrum is simply the convolution of a stellar spectrum with a Gaussian distribution which describes the line-of-sight velocity dispersion of the galaxy's constituent stars. The object you

---

[1]http://pysalt.salt.ac.za/

[2]http://iraf.noao.edu/

want to determine the redshift of and a spectral template (of that class of object at rest frame) are filtered in Fourier space and multiplied together to form the transform of the cross-correlation function. This transform of the cross-correlation function is then transformed back into real space. Cross-correlating a template spectrum with the galaxy spectrum produces a function with a peak at the redshift of the galaxy with a width related to the dispersion of the galaxy. A description and summary of settings for this task are in the appendix.

I used six different SDSS DR2 galaxy templates to cross-correlate[3]. I ran the cross-correlation repeatedly, with starting redshifts spanning $0.0 < z < 1$ in intervals of $\delta z = 0.0001$ for each template. The redshift with the highest correlation coefficient was selected as the best measurement for that template. This method provided six possible redshifts (one from each template). These six highest-correlation-redshifts were manually inspected by myself and two or more other reviewers to select the optimal redshift. The spectral features in the object spectrum were confirmed in the 2d spectral image by visual inspection. Note the the errors reported in XCSAO are not stated here since they are known to be severely underestimated. To get a true error we would need to measure the same galaxy z multiple times (which is currently unavailable). However, the z values reported here are certainly accurate to the 3rd decimal place.

I defined a quality rating system (Q) to describe the confidence level of each redshift measurement (Wirth et al., 2004). Galaxies exhibiting multiple absorption and (or) emission features were given a $Q = 4$ rating; galaxies exhibiting a single, strongly detected feature were a $Q = 3$ rating; galaxies showing the proper z range but exhibiting no strong features were $Q = 2$; and galaxies showing erroneous z values and no strong features were rated $Q = 1$.

3.3.2 SALT RSS Performance

Only those redshift measurements rated $Q = 3$ or greater were selected for cluster analysis and therefore were considered a successful observation (Fig 3.1).

Of all the observed galaxies, only those with a $Q \geq 3$ were included in the sample used to measure cluster velocity dispersions, as described in Section 3 below. These galaxies account

---

[3]http://www.sdss.org/dr7/algorithms/spectemplates/index.html
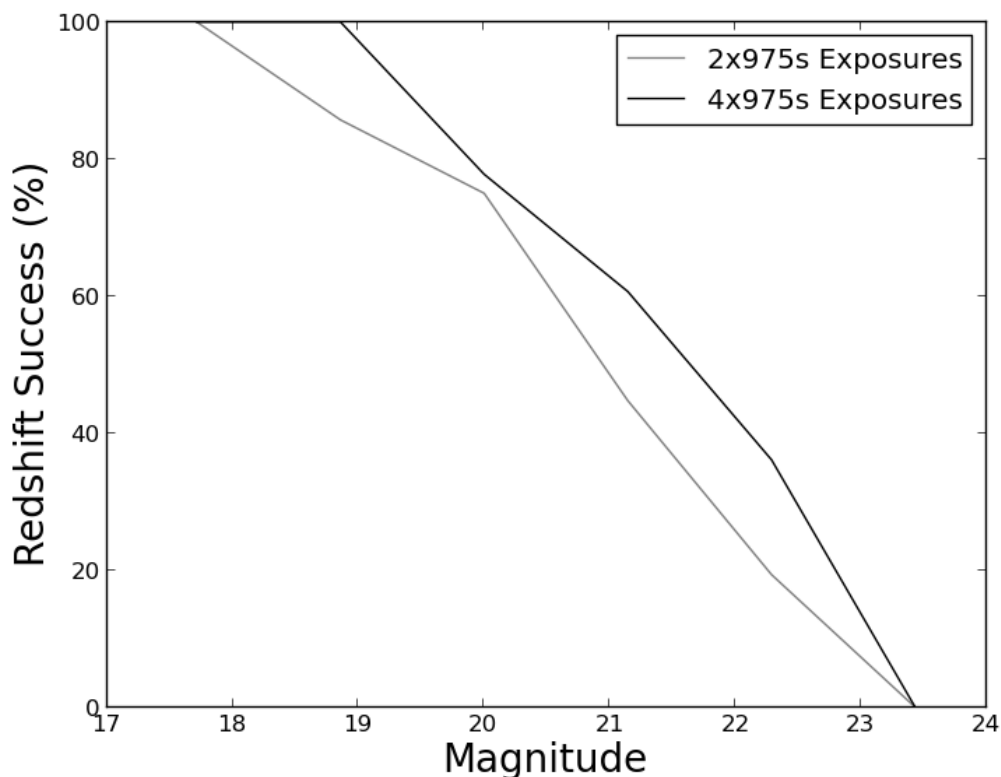
Figure 3.1: The percent of spectra resulting in a Q = 3 or greater out of all observed galaxies for given magnitude and exposure time.

for 205 of the 373 observed galaxies, which represents 55 per cent of all targeted objects. These targets spanned the *r*-band magnitude range of 17 - 22.5. In our observing program we used multiple integration times. Our 2×975s exposures have a 54 per cent success rate spanning the *r*-band magnitude range of 17 - 22.3 while the 4×975s exposures resulted in a 56 per cent success rate spanning the *r*-band magnitude range of 18 - 22.5.

3.3.3 Cluster Redshift Measurements

In order to determine the cluster redshift I only considered those galaxies with rating $Q = 3$ or greater to be in the sample. To determine the cluster redshift I used the biweight location method proposed by Beers et al. (1990). The biweight location estimator is used for non-Gaussian or

contaminated norma distributions, and comes from the broad family of estimators known as *M* estimators of location. The defining characteristic of *M* estimators is the minimization of a function of the deviates of each observation from the estimate of location. The median absolute deviation (MAD) is a measure of statistical dispersion that is resilient to outliers in a data set. In the standard deviation, the distances from the mean are squared, so large deviations are weighted more heavily, and thus outliers can heavily influence it. In the MAD, the deviations of a small number of outliers are irrelevant. The MAD is defined as

$$MAD = median(|x_i - M|). \tag{3.1}$$

Therefore the definition of the biweight location estimator is

$$C_{BI} = M + \frac{\Sigma_{|u_i|<1}(x_i - M)(1 - u_i^2)^2}{\Sigma_{|u_i|<1}(1 - u_i^2)^2}, \tag{3.2}$$

where *M* is the sample median and u_i are given by

$$u_i = \frac{(x_i - M)}{cMAD}. \tag{3.3}$$

The constant *c* is known as the "tuning constant" and is chosen to give C_{BI} high efficiency for a broad range of distributions. The best balance of efficiency for location estimation is found for $c = 6.0$, which includes data up to four standard deviations from the central location (Mosteller & Tukey, 1977).

Since all of our clusters are located within the SDSS footprint, we added SDSS DR10 (Ahn et al., 2014) redshifts for galaxies located within a 12' search box centred on each cluster position. We took care to ensure that we did not include SDSS redshifts that were duplicated in our SALT observations. There were 11 such galaxies that had SDSS redshifts, when compared to SALT redshifts the median $\delta_z = 3 \times 10^{-5}$.

I took the biweight location (Beers et al., 1990) of the sample and removed any obvious foreground and background galaxies by applying a 3000 km s^{-1} cut relative to the biweight location. I removed any cluster interlopers (as explained below) and the biweight location was then recalculated from the remaining galaxies. The whole sample of $Q = 3$ or greater galaxies

was measured again relative to the new biweight location. This process was repeated until the *z* value for the cluster converged. I use this value as the new redshift around which to calculate peculiar velocities of possible cluster members. We adopt the coordinates of the BCG as the position of the cluster center.

3.3.4 Determining Cluster Membership

Not all of the galaxies targeted in the SALT RSS field of view are identified as cluster members. For this work, I used an adaptation of the fixed-gap method to identify members. This is similar to the procedure used by (Fadda et al., 1996) and further refined in (Crawford et al., 2014). I define the peculiar velocity of a galaxy within a cluster as

$$\Delta v_i = c \frac{(z_i - \bar{z})}{(1 + \bar{z})} \tag{3.4}$$

where Δv_i is the peculiar velocity of the *i*th galaxy, z_i is its redshift, and $\bar{z}$ is the redshift of the cluster as estimated using the biweight location. To find the interlopers I sorted all galaxies by their velocities and identified any adjacent galaxies (in velocity space) with gaps greater than 1000 km s^{-1} [4]. I iteratively remove galaxies with gaps of greater than 1000 km s^{-1} compared to their neighbor until the number of galaxies in the cluster remains constant. Any galaxies that fall outside R_{200c}, the radius at which the mean density is 200 times the critical density of the Universe, were not considered as part of the virialized cluster and therefore rejected. The R_{200c} radius is calculated using M_{200c} and assumes spherical clusters (i.e, $M_{200c} = 200\rho_c \times 4\pi R_{200c}^3/3$).

.

3.3.5 Determining Velocity Dispersion and Mass

The galaxies remaining at this point were considered members of the cluster. I used the biweight scale estimator of (Beers et al., 1990) to calculate the cluster velocity dispersion from the galaxies selected as members. With the velocity dispersions in hand, I calculated the dynamical masses.

---

[4]De Propris et al. (2003) argue that galaxy clusters correspond to well-defined peaks with respect to recessional velocity and that gaps between successive galaxies of more than 1000 km s^{-1} indicate interlopers)

Following Sifón et al. (2012), I estimated the dynamical masses of the clusters by applying the scaling relation of Evrard et al. (2008), which is derived from cosmological, dark matter only, N-body simulations. These massive dark matter halos adhere to a virial scaling relation of the form

$$\sigma_{DM}(M,z) = \sigma_{DM,15} \left[\frac{h(z)M_{200c}}{10^{15}M_{\odot}} \right]^{\alpha}, \tag{3.5}$$

where

$$h(z) = \frac{H_0 \sqrt{\Omega_m(1+z)^3 + \Omega_{\Lambda}}}{100}. \tag{3.6}$$

M_{200c} (M_{500c}) is mass measured within R_{200c} (R_{500c}), which is the radius at which the mean density is 200 (500) times the critical density of the Universe at the cluster redshift. $H_0 = 70$ km s^{-1} Mpc^{-1}, $\sigma_{DM,15}$ is the normalization at mass $10^{15}h^{-1}$ M$_{\odot}$, and α is the logarithmic slope; $\sigma_{DM,15} = 1082.9 \pm 4.0$ km s^{-1} and $\alpha = 0.3361 \pm 0.0026$ ((Evrard et al., 2008)). All errors have been estimated by the bootstrap re-sampling technique with 5000 iterations. We assume these galaxies are unbiased tracers of the mass in the cluster. While this is probably a reasonable assumption we have not investigated possible biases between the dark matter and the galaxies as velocity tracers. Others (e.g., Old et al., 2013) are currently investigating this using numerical simulations.

3.4 Results

The results for the clusters are shown in Table 3.2. Table 3.2 lists the cluster ID, number of members, redshifts, velocity dispersion, $r200_c$, and M_{500c}.

A sample of spectra and their respective templates can be seen in Figures 3.2 - 3.7. In these figures the left hand panel shows a 9×9 arcmin false color SDSS optical image (g, r, i). Objects highlighted in cyan are confirmed members for which a selection of the corresponding spectra are shown in the right hand panel; red circles mark all other spectroscopically confirmed galaxies that have been identified as non-members or interlopers. Only objects with secure redshifts ($Q = 3$

Table 3.2: SZE-derived mass estimates for the ACT selected clusters. The numbers listed in brackets in the Members column are those added from the DR10 data. The Y_{500c} values are from Hasselfield et al. (2013). Note: the mass quoted for ACT-CL J0156.4-0123 is stated only for completeness.

Cluster ID	Members [DR10]	z	σ_v (km s^{-1})	R_{200c} (Mpc)	M_{200c} (10^{14} M$_\odot$)	Y_{500c} (10^{-4} arcmin^2)
ACT-CL J0320.4+0032	27 [5]	0.3838	1432 ± 157	2.5	26.9 ± 7.6	2.8 ± 0.9
ACT-CL J0348.6-0028	22 [0]	0.3451	866 ± 152	1.6	6.1 ± 2.1	2.6 ± 1.0
ACT-CL J0342.7-0017	16 [7]	0.3069	1057 ± 168	1.9	11.4 ± 4.5	3.2 ± 1.2
ACT-CL J2058.8+0123	14 [0]	0.3273	936 ± 115	1.7	7.8 ± 2.5	7.8 ± 1.4
ACT-CL J0219.9+0129	13 [5]	0.3655	900 ± 210	1.6	6.8 ± 4.7	2.3 ± 0.9
ACT-CL J0045.2-0152	12 [4]	0.5493	1068 ± 266	1.7	10.2 ± 5.5	4.8 ± 0.9
ACT-CL J0156.4-0123	4 [1]	0.4569	660 ± 134	1.1	2.6 ± 1.2	2.1 ± 0.8

or greater; see Fig 3.1) are plotted. In the right hand panel, a selection of spectra spanning the magnitude range of the members are shown as indicated in the figure, and the spectrum for the brightest object is that of the BCG. The black line is the SALT RSS spectra and the red line is the SDSS spectral template. We find the spectrum of the Brightest Cluster Galaxy in ACT-CL J0320.4+0032 shows strong emission line features and therefore suggests an active galactic nucleus (AGN) is present. Spitzer's Infrared Array Camera (IRAC) has magnitudes of the BCG at 3.6 and 4.5 microns with AB magnitude values of 17.724 ± 0.004 and 17.850 ± 0.004 respectively (measured by Dr Matthew Hilton). These AB magnitudes are aperture corrected; for more information on the data processing and photometry refer to Hilton et al. (2013). The [3.6]-[4.5] micron colour of the BCG is -0.13 ± 0.06, hence these data further supports the idea the BCG contains an active galactic nucleus (see Figure 6 of Hilton et al. 2010). This may be an example of a very massive cluster in which AGN feedback is taking place.

In the Appendix the individual SALT galaxy ID's, RA, Dec, magnitude, spectroscopic z, Q-rating, emission line status, membership status, and distance from the BCG can be seen for each
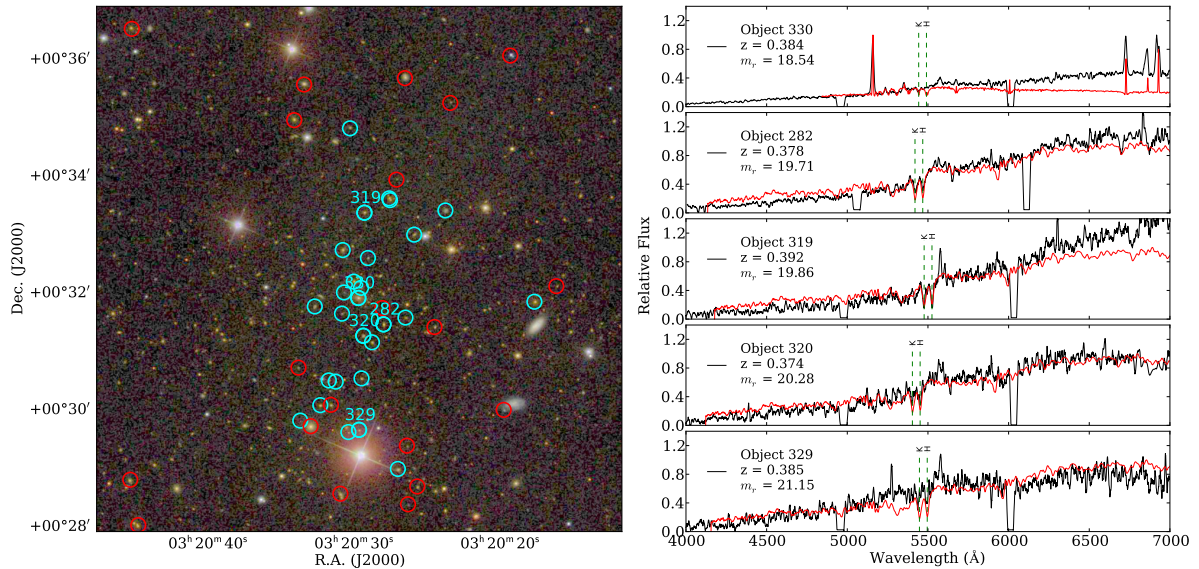
Figure 3.2: The $z = 0.38$ cluster ACT-CL J0320.4+0032. The left hand panel shows a 9 by 9 arcmin false color SDSS optical image (g, r, i). Objects highlighted in cyan are spectroscopically confirmed members (see Section 3.3.4; spectra for objects marked with ID numbers are shown in the right hand panel); red circles mark non-members and interloper galaxies with confirmed redshifts. Only objects with secure redshifts ($Q = 3$ or greater; see Section 3.3.1) are plotted. In the right hand panel, black lines correspond to SALT RSS spectra, while red lines show the best match redshifted SDSS spectral template in each case. The displayed object spectra span a representative range in r-band magnitudes, as indicated in the figure, and the spectrum for the brightest object is that of the BCG.
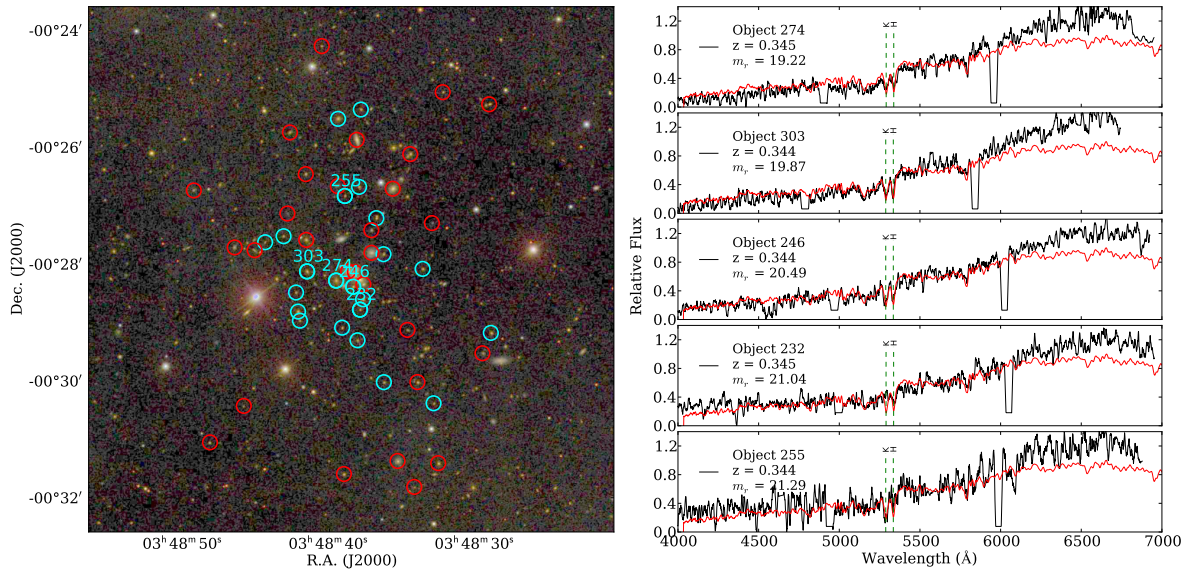
Figure 3.3: The $z = 0.35$ cluster ACT-CL J0348.6-0028 (see Fig. 3.2 for an explanation of symbols and colors).
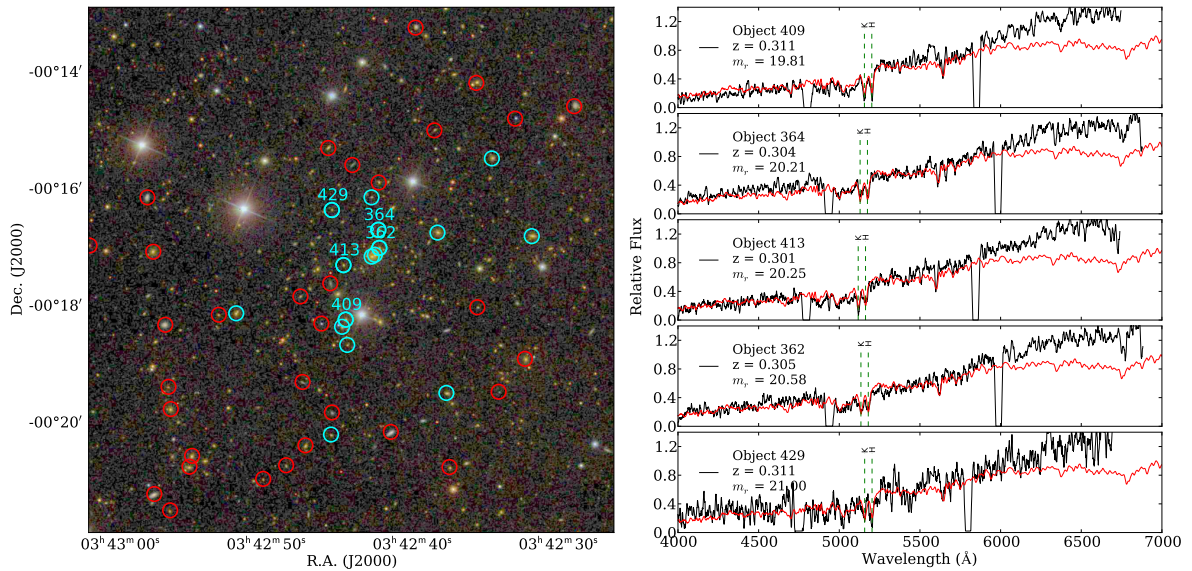
Figure 3.4: The $z = 0.30$ cluster ACT-CL J0342.7-0017 (see Fig. 3.2 for an explanation of symbols and colors).
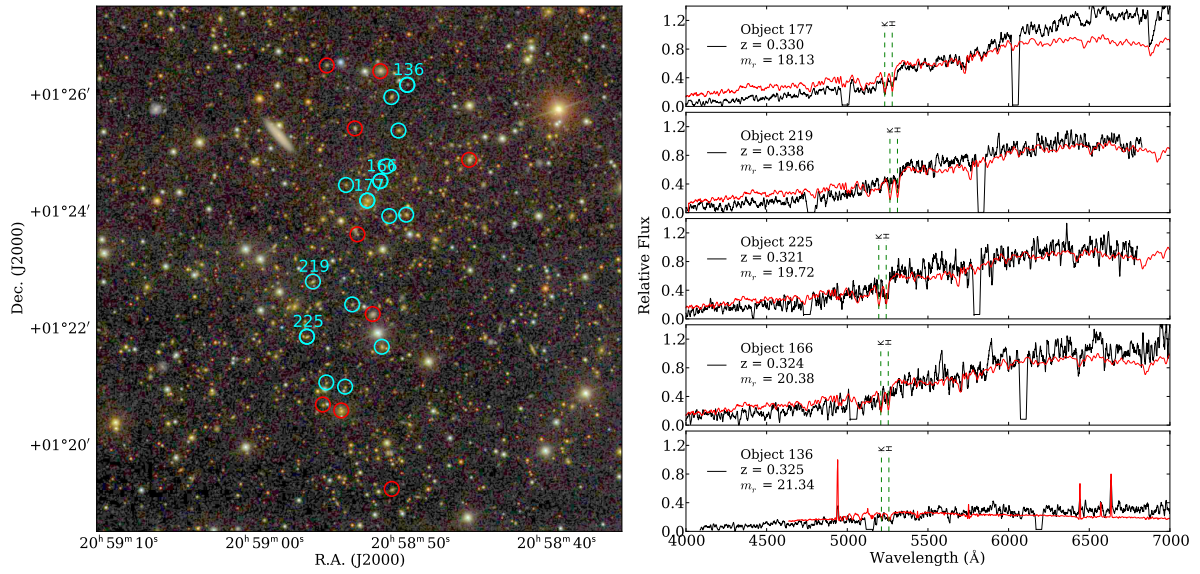
Figure 3.5: The $z = 0.33$ cluster ACT-CL J2058.8+0123 (see Fig. 3.2 for an explanation of symbols and colors).
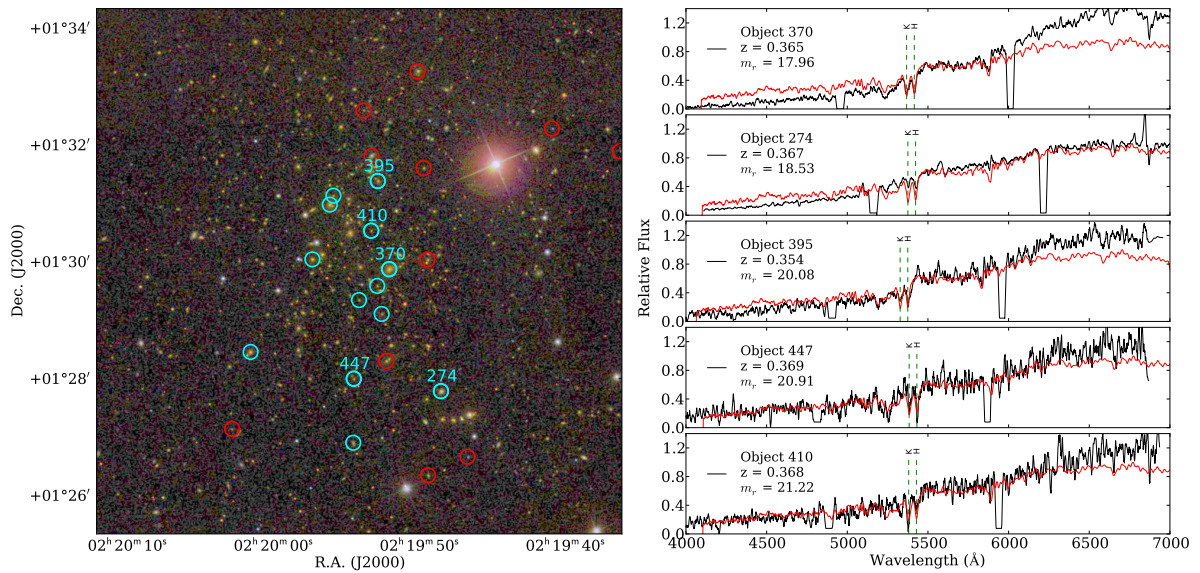
Figure 3.6: The $z = 0.36$ cluster ACT-CL J0219.4+0129 (see Fig. 3.2 for an explanation of symbols and colors).

36
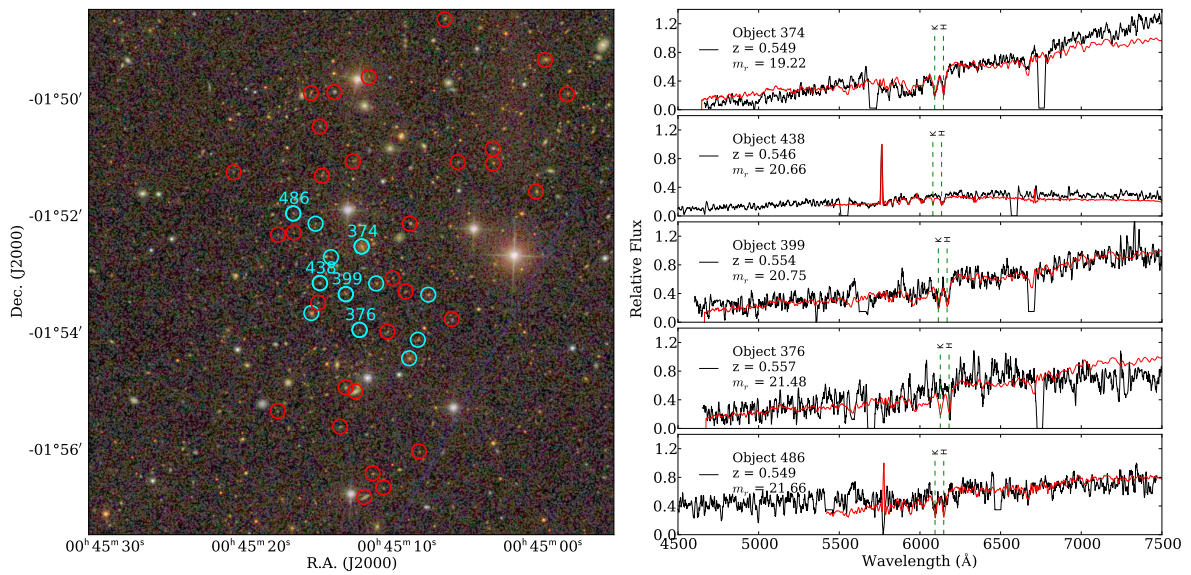
Figure 3.7: The $z = 0.55$ cluster ACT-CL J0045.2-0152 (see Fig. 3.2 for an explanation of symbols and colors).
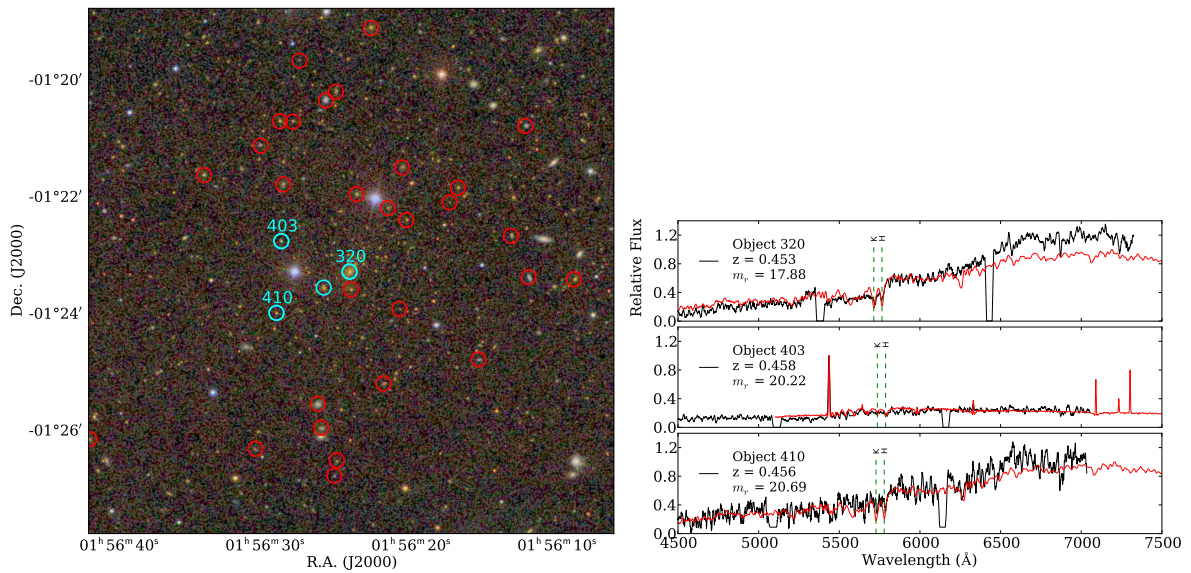
Figure 3.8: The $z = 0.46$ cluster ACT-CL J0156.4-0123 (see Fig. 3.2 for an explanation of symbols and colors) The unlabeled galaxy is from SDSS DR10.

galaxy.

Discussion

4.1 Previous Dynamical Mass Results

We compare our results with those from (Sifón et al., 2012). Sifón et al. (2012) estimated dynamical masses on a sample of 16 clusters also detected by ACT, with a procedure very similar to ours. R_{200c}, the radius at which the overdensity in the cluster is 200 times the critical density, was estimated from their dynamical mass and used to measure Y_{200}. Their sample ranges from $0.28 \leq z \leq 1.07$ with a median redshift of $z = 0.50$, where each cluster has ≈ 60 galaxy members (Section 2.2.3). We compare our cluster results to those in (Sifón et al., 2012); when comparing we converted Sifon's cluster values from M_{200c} (R_{200c}) to M_{500c} (R_{500c}). For the conversion we assumed the concentration-mass relation from (Duffy et al., 2008) and integrated over a Navarro-Frenk-White (NFW) profile (Navarro et al., 1997). The mass values derived in this work are in good general agreement with the cluster values of (Sifón et al., 2012) given the scatter. A plot of our results and the values from (Sifón et al., 2012) can be seen in Figure 4.1. It is worth mentioning the most-massive SALT cluster in our sample is ACT-CL J0320.5+0032, host to the AGN discussed earlier in this section.

4.2 SZE-Mass Scaling Relations

Given an accurate calibration of the SZE-Mass scaling relation Vanderlinde et al. (2010) and Sehgal et al. (2011) have shown the inclusion of the ACT cluster samples can lead to significant improvements in the uncertainties of cosmological parameters, particularly Ω_{mass} and $\sigma 8$, over WMAP-7-only constraints. Y-M relations from the work discussed in Section 2 are show in Figure 4.1.

The two relations based on data come from Sifón et al. (2012) and Marrone et al. (2012). Sifón et al. (2012) present a scaling relation from comparing SZE fluxes and masses derived from dynamical information. Their sample has a median redshift of $z = 0.50$ and median mass of $M_{200c} \simeq 12 \times 10^{14} h_{70}^{-1} M_\odot$. I note that the Sifon line has been shifted from the Y200-M200 relation and is somewhat sensitive to the assumptions about the relationship between Y200 and Y500.

Marrone et al. (2012) present the second data-derived Y-M relation. Their relation is based on weak-lensing measurements of a sample of 18 galaxy clusters from the LoCuSS "high-L_x" sample (a sub-sample of the ROSAT survey). The Marrone et al. (2012) fit from weak lensing results is somewhat lower than that obtained from other methods. For a direct comparison to our study, this offset is possibly due to our limited spatial coverage of galaxy redshifts. This limited coverage only allows us to measure galaxies near the cluster center which inevitably have higher velocities and therefore higher mass. Marrone et al. (2012) also note the uncertainties in calculating spherical masses from their 2-dimensional weak lensing measurements. This introduces bias to their weak-lensing masses and therefore their relations.

The simulation derived relation came from Battaglia et al. (2012). They present a hydrodynamical-simulation-based scaling relation between mass and SZE. The relation is based on the self-similar scaling relation of the idealized case of a cluster in virial equilibrium: shock heating, radiative cooling, and AGN feedback are not taken into account in the chosen relation. The values for the latter are the results at $z = 0.5$, which corresponds closer to the characteristic redshift of our sample. It is possible that given that our sample of clusters includes emission line galaxies and at least one cluster with on-going feedback the idealized relation may not be an adequate

assumption for our sample.

Arnaud et al. (2010) present an X-ray-temperature-based scaling relation between X-ray luminosity and SZE. The SZE signal is calculated from X-ray gas properties and is not a scaling law derived from data. Their sample consists of 33 clusters from the REFLEX catalogue and are observed with XMM-Newton. The sample spans a mass range of 10^{14} M$_\odot$ < M$_{500c}$ < 10^{15} M$_\odot$ within $z < 0.2$. It has been noted in Marrone et al. (2012) that X-ray scaling relations are typically constructed from hydrostatic-equilibrium-based masses. These HSE-based mass scaling relations are plagued by varying degrees of correlation that depend on the details of the measurement methods Mantz et al. (2010).

The masses calculated from our observations and Sifon's study both generally lie above the relations derived by (Marrone et al., 2012), (Arnaud et al., 2010), and (Battaglia et al., 2012). Since a similar offset is apparent in both dynamical mass measurements we speculate this difference is related to the observing properties the cluster mass (and relations) are derived from. As previously stated, for dynamical measurements, limited spatial coverage of galaxy redshift measurements only allows for members near the cluster center to be observed. This effect biases the velocity dispersions to be higher and therefore biases the mass to be higher. The ideal scaling relations measurement would be one that compares two observables that have been derived independently. By combining multiple approaches one can understand the underlying systematics and tighten the Y-M relation, leading to more powerful constraints on cosmological parameters.
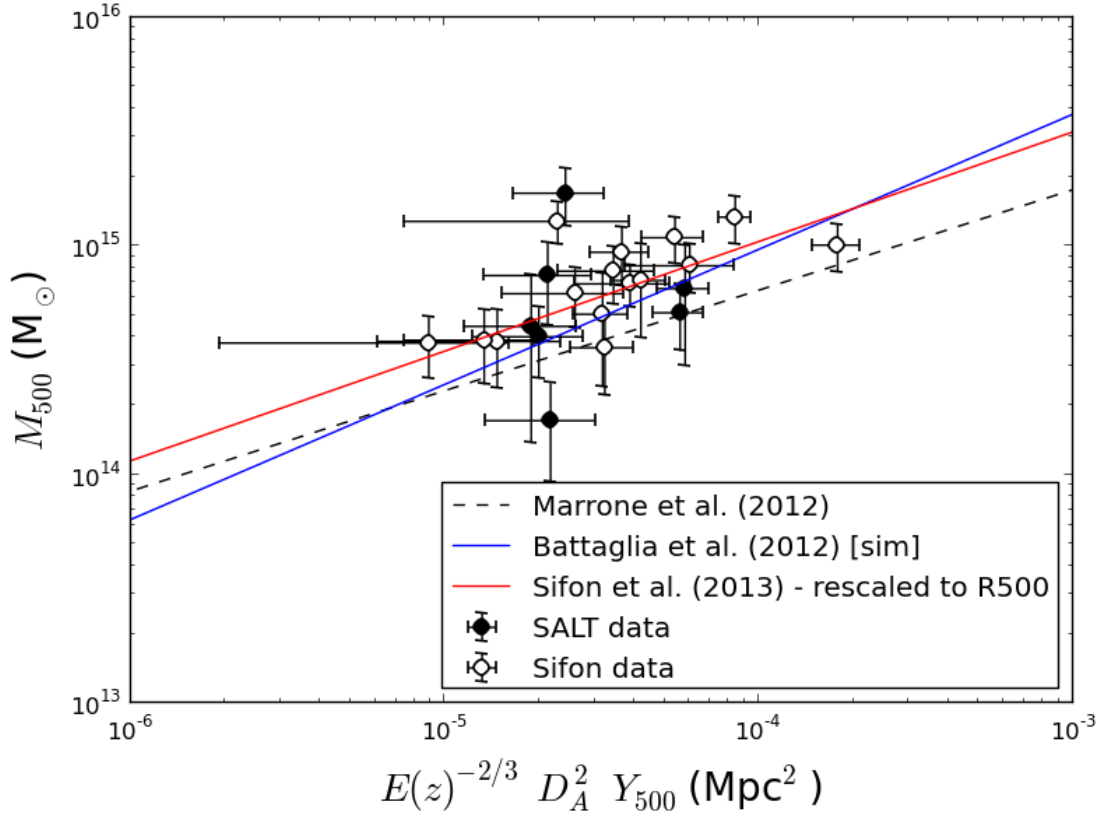
Figure 4.1: Plot of SALT derived masses and Sifón et al. (2012) masses over SZE scaling relations. Estimators have been scaled as indicated in the axis labels. The x-axis is the correlated Y-value for a cluster at $R500c$. The y-axis is $M500c$. Sifon et al's cluster results are circles and SALT-observed cluster results are black dots. Previous estimates of the $Y - M$ scaling relation are shown with dashed, blue, and red lines (see text for details).

CHAPTER 5

Conclusion

We have conducted a spectroscopic follow-up program of clusters of galaxies discovered via the Sunyaev-Zel'dovich effect by the ACT in its equatorial strip survey. We used multi-object spectroscopic observations from the Southern African Large Telescope. From our SALT spectroscopic data we have: (i) extracted individual galaxy redshifts, (ii) determined which galaxies are cluster members, and from the members we have (iii) measured the cluster redshifts, (iv) measured the cluster velocity dispersions and hence (v) determined the cluster dynamical masses. The dynamical masses have been estimated from the radial velocity dispersions using the (Evrard et al., 2008) simulation based σ - M200c scaling relation. These clusters range in masses from 2.6×10^{14} M$_\odot$ to 2.6×10^{15} M$_\odot$ and span a redshift range of $z = 0.3$ to $z = 0.55$. Our results, and those from (Sifón et al., 2012), will be added to the future Sifón et al. (in prep.) to present an updated measurement of the Sunyaev-Zel'Dovich-mass scaling relation. This study has also proved to be a successful early use of SALT for extragalactic astronomy. These results, as well as continued efforts to improve the telescope and instrument performance, justify a more extensive use of SALT in the future for exploring higher z clusters.

43

Appendix

A.1 Tables

Table A1: Spectroscopic redshifts of galaxies in the direction of ACT-CL J0045.2-0152 measured using SALT RSS; m_r is the SDSS r-band magnitude of the object; z is the redshift; Q is the redshift quality flag (see Section 3.3.1); Em. Lines? indicates objects which show emission lines in their spectra (e.g., OII 3727 AA); Member? indicates objects which are determined to be cluster members (see Section 3.3.4); r (Mpc) indicates the projected distance from the ACT cluster position as given by Hasselfield et al. (2013).

ID	Mask	RA (J2000)	Dec. (J2000)	m_r	z	Q	Em. Lines?	Member?	r (Mpc)
399	1	$00^h45^m13\overset{s}{.}586$	$-01°53'20\overset{''}{.}61$	20.75	0.554	4	✓	✓	0.15
418	1	$00^h45^m14\overset{s}{.}607$	$-01°52'42\overset{''}{.}69$	21.98	0.548	4	...	✓	0.16
374	1	$00^h45^m12\overset{s}{.}499$	$-01°52'31\overset{''}{.}65$	19.22	0.549	4	...	✓	0.18
438	1	$00^h45^m15\overset{s}{.}359$	$-01°53'09\overset{''}{.}28$	20.66	0.546	4	✓	✓	0.22
326	2	$00^h45^m10\overset{s}{.}374$	$-01°53'04\overset{''}{.}29$	21.70	0.565	3	...	...	...

Table A1 – continued from previous page

ID	Mask	RA (J2000)	Dec. (J2000)	m_r	z	Q	Em. Lines?	Member?	r (Mpc)
440	2	$00^h45^m15\overset{s}{.}476$	$-01°53'29\overset{''}{.}43$	21.38	0.488	4	✓	...	...
451	1	$00^h45^m15\overset{s}{.}949$	$-01°53'40\overset{''}{.}05$	19.88	0.553	4	...	✓	0.38
306	2	$00^h45^m09\overset{s}{.}483$	$-01°53'17\overset{''}{.}99$	21.47	0.990	4	...	...	...
376	1	$00^h45^m12\overset{s}{.}645$	$-01°53'57\overset{''}{.}37$	21.48	0.557	3	...	✓	0.39
446	1	$00^h45^m15\overset{s}{.}661$	$-01°52'08\overset{''}{.}31$	21.99	0.550	4	...	✓	0.39
485	2	$00^h45^m17\overset{s}{.}147$	$-01°52'17\overset{''}{.}38$	21.82	0.528	3	✓	...	...
335	2	$00^h45^m10\overset{s}{.}733$	$-01°53'59\overset{''}{.}12$	21.66	0.628	4	...	...	...
509	1	$00^h45^m18\overset{s}{.}228$	$-01°52'19\overset{''}{.}59$	21.93	0.710	4	✓	...	...
486	2	$00^h45^m17\overset{s}{.}187$	$-01°51'57\overset{''}{.}75$	21.66	0.549	4	...	✓	0.54
434	2	$00^h45^m15\overset{s}{.}222$	$-01°51'18\overset{''}{.}97$	21.33	0.572	3	...	...	...
387	1	$00^h45^m13\overset{s}{.}094$	$-01°51'04\overset{''}{.}19$	21.45	0.513	4	✓	...	...
251	2	$00^h45^m06\overset{s}{.}334$	$-01°53'46\overset{''}{.}27$	21.34	0.642	3	✓	...	...
400	1	$00^h45^m13\overset{s}{.}59$	$-01°54'56\overset{''}{.}36$	20.47	0.367	3	...	...	...
439	1	$00^h45^m15\overset{s}{.}372$	$-01°50'28\overset{''}{.}54$	21.44	0.657	4	✓	...	...
240	2	$00^h45^m05\overset{s}{.}910$	$-01°51'05\overset{''}{.}14$	21.50	0.944	4	...	...	...
555	1	$00^h45^m21\overset{s}{.}277$	$-01°51'15\overset{''}{.}53$	21.57	0.689	4	✓	...	...
407	1	$00^h45^m13\overset{s}{.}979$	$-01°55'36\overset{''}{.}78$	20.98	0.672	3	...	...	...
510	2	$00^h45^m18\overset{s}{.}243$	$-01°55'20\overset{''}{.}68$	21.61	0.528	3	✓	...	...
415	1	$00^h45^m14\overset{s}{.}368$	$-01°49'53\overset{''}{.}20$	20.15	0.243	4	✓	...	...
207	1	$00^h45^m03\overset{s}{.}524$	$-01°50'51\overset{''}{.}21$	20.18	0.473	4	...	...	...
293	2	$00^h45^m08\overset{s}{.}572$	$-01°56'02\overset{''}{.}23$	21.79	0.295	3	...	...	...
363	1	$00^h45^m12\overset{s}{.}009$	$-01°49'37\overset{''}{.}58$	21.18	0.543	4	...	...	...
355	1	$00^h45^m11\overset{s}{.}751$	$-01°56'24\overset{''}{.}72$	21.26	0.552	4	✓	...	...
343	1	$00^h45^m11\overset{s}{.}012$	$-01°56'39\overset{''}{.}24$	21.58	0.201	4	...	...	...
371	2	$00^h45^m12\overset{s}{.}315$	$-01°56'48\overset{''}{.}94$	19.37	0.827	4	...	...	...

Table A2: Spectroscopic redshifts of galaxies in the direction of ACT-CL
J0156.4-0123 measured using SALT RSS; see Table A1 for an explana-
tion of the table columns.

ID	Mask	RA (J2000)	Dec. (J2000)	m_r	z	Q	Em. Lines?	Member?	r (Mpc)
320	1	$01^h56^m24\overset{s}{.}297$	$-01°23'17\overset{''}{.}32$	17.88	0.453	4	...	✓	0.01
317	1	$01^h56^m24\overset{s}{.}192$	$-01°23'35\overset{''}{.}61$	20.34	0.438	4	...	...	...
246	3	$01^h56^m20\overset{s}{.}883$	$-01°23'55\overset{''}{.}64$	21.45	0.597	3	...	...	...
268	1	$01^h56^m21\overset{s}{.}674$	$-01°22'12\overset{''}{.}07$	21.08	0.444	4	✓	...	...
239	1	$01^h56^m20\overset{s}{.}400$	$-01°22'24\overset{''}{.}40$	20.78	0.569	4	...	...	...
403	1	$01^h56^m28\overset{s}{.}970$	$-01°22'46\overset{''}{.}03$	20.22	0.458	4	✓	✓	0.45
310	1	$01^h56^m23\overset{s}{.}810$	$-01°21'57\overset{''}{.}79$	19.71	0.277	4	...	...	...
410	1	$01^h56^m29\overset{s}{.}305$	$-01°23'59\overset{''}{.}72$	20.69	0.456	4	...	✓	0.51
243	1	$01^h56^m20\overset{s}{.}696$	$-01°21'30\overset{''}{.}28$	19.90	0.560	4	✓	...	...
195	3	$01^h56^m17\overset{s}{.}450$	$-01°22'06\overset{''}{.}30$	21.92	0.599	3	✓	...	...
186	3	$01^h56^m16\overset{s}{.}882$	$-01°21'51\overset{''}{.}12$	20.06	0.568	4	...	...	...
361	1	$01^h56^m26\overset{s}{.}472$	$-01°25'33\overset{''}{.}21$	18.22	0.137	4	✓	...	...
419	1	$01^h56^m30\overset{s}{.}384$	$-01°21'07\overset{''}{.}92$	20.60	0.680	4	✓	...	...
164	1	$01^h56^m15\overset{s}{.}462$	$-01°24'47\overset{''}{.}50$	20.03	0.606	4	✓	...	...
355	1	$01^h56^m26\overset{s}{.}243$	$-01°25'57\overset{''}{.}64$	19.66	0.340	4	✓	...	...
393	1	$01^h56^m28\overset{s}{.}181$	$-01°20'43\overset{''}{.}36$	20.68	0.394	4	...	...	...
142	3	$01^h56^m13\overset{s}{.}247$	$-01°22'40\overset{''}{.}53$	19.98	0.771	3	✓	...	...
350	3	$01^h56^m25\overset{s}{.}923$	$-01°20'21\overset{''}{.}53$	18.60	0.381	4	✓	...	...
468	3	$01^h56^m34\overset{s}{.}261$	$-01°21'38\overset{''}{.}25$	19.58	0.340	4	...	...	...
123	3	$01^h56^m12\overset{s}{.}040$	$-01°23'23\overset{''}{.}13$	19.12	0.477	4	✓	...	...
337	1	$01^h56^m25\overset{s}{.}235$	$-01°20'12\overset{''}{.}52$	20.15	0.039	4	...	...	...
335	1	$01^h56^m25\overset{s}{.}171$	$-01°26'31\overset{''}{.}22$	20.65	0.455	4	...	...	...
426	1	$01^h56^m30\overset{s}{.}748$	$-01°26'19\overset{''}{.}24$	20.93	0.450	4	...	...	...
340	1	$01^h56^m25\overset{s}{.}337$	$-01°26'46\overset{''}{.}89$	21.09	0.736	4	✓	...	...
385	3	$01^h56^m27\overset{s}{.}728$	$-01°19'40\overset{''}{.}68$	21.59	0.385	3	...	...	...
127	3	$01^h56^m12\overset{s}{.}255$	$-01°20'47\overset{''}{.}78$	19.70	0.421	3	✓	...	...

Table A3: Spectroscopic redshifts of galaxies in the direction of ACT-CL J0219.9+0129 measured using SALT RSS; see Table A1 for an explanation of the table columns.

ID	Mask	RA (J2000)	Dec. (J2000)	m_r	z	Q	Em. Lines?	Member?	r (Mpc)
397	1	$02^h19^m52\overset{s}{.}975$	$+01°29'35\overset{''}{.}03$	21.29	0.364	4	...	✓	0.12
434	1	$02^h19^m54\overset{s}{.}222$	$+01°29'20\overset{''}{.}51$	21.01	0.364	4	...	✓	0.15
370	1	$02^h19^m52\overset{s}{.}155$	$+01°29'52\overset{''}{.}19$	17.96	0.365	4	...	✓	0.15
410	1	$02^h19^m53\overset{s}{.}386$	$+01°30'31\overset{''}{.}71$	21.22	0.368	4	...	✓	0.21
390	1	$02^h19^m52\overset{s}{.}668$	$+01°29'06\overset{''}{.}20$	21.01	0.358	4	...	✓	0.25
508	1	$02^h19^m55\overset{s}{.}973$	$+01°31'07\overset{''}{.}71$	21.23	0.365	4	...	✓	0.40
395	1	$02^h19^m52\overset{s}{.}931$	$+01°31'22\overset{''}{.}76$	20.08	0.354	4	...	✓	0.47
379	1	$02^h19^m52\overset{s}{.}348$	$+01°28'17\overset{''}{.}92$	20.17	0.350	4	...	...	...
447	1	$02^h19^m54\overset{s}{.}580$	$+01°27'59\overset{''}{.}68$	20.91	0.369	4	...	✓	0.55
407	1	$02^h19^m53\overset{s}{.}365$	$+01°31'48\overset{''}{.}61$	19.11	0.239	4	...	...	...
309	1	$02^h19^m49\overset{s}{.}797$	$+01°31'35\overset{''}{.}97$	20.67	0.349	4	...	...	...
274	1	$02^h19^m48\overset{s}{.}609$	$+01°27'46\overset{''}{.}90$	18.53	0.367	4	...	✓	0.74
428	1	$02^h19^m53\overset{s}{.}908$	$+01°32'35\overset{''}{.}19$	21.45	0.560	4	...	...	...
450	1	$02^h19^m54\overset{s}{.}615$	$+01°26'53\overset{''}{.}96$	20.06	0.370	4	...	✓	0.87
663	1	$02^h20^m02\overset{s}{.}912$	$+01°27'08\overset{''}{.}25$	21.69	0.358	3	...	...	...
229	1	$02^h19^m46\overset{s}{.}790$	$+01°26'39\overset{''}{.}57$	21.61	0.786	4	✓	...	...
299	1	$02^h19^m49\overset{s}{.}495$	$+01°26'20\overset{''}{.}61$	20.68	0.531	4	✓	...	...

Table A4: Spectroscopic redshifts of galaxies in the direction of ACT-CL J0320.4+0032 measured using SALT RSS; see Table A1 for an explanation of the table columns.

ID	Mask	RA (J2000)	Dec. (J2000)	m_r	z	Q	Em. Lines?	Member?	r (Mpc)
311	2	$03^h20^m29\overset{s}{.}130$	$+00°32'34\overset{''}{.}61$	21.02	0.379	4	✓	✓	0.07
324	2	$03^h20^m29\overset{s}{.}602$	$+00°32'03\overset{''}{.}99$	21.73	0.388	4	...	✓	0.10
356	3	$03^h20^m30\overset{s}{.}772$	$+00°31'59\overset{''}{.}27$	21.92	0.394	4	...	✓	0.15
330	1	$03^h20^m29\overset{s}{.}788$	$+00°31'53\overset{''}{.}60$	18.54	0.384	4	...	✓	0.16

Table A4 – continued from previous page

ID	Mask	RA (J2000)	Dec. (J2000)	m_r	z	Q	Em. Lines?	Member?	r (Mpc)
286	2	$03^h20^m28\overset{s}{.}141$	$+00°31'43\overset{''}{.}24$	22.06	0.472	3	...	...	...
360	1	$03^h20^m30\overset{s}{.}907$	$+00°31'37\overset{''}{.}50$	21.75	0.383	3	...	✓	0.26
319	1	$03^h20^m29\overset{s}{.}372$	$+00°33'21\overset{''}{.}18$	19.86	0.392	4	...	✓	0.30
396	3	$03^h20^m32\overset{s}{.}770$	$+00°31'44\overset{''}{.}87$	20.32	0.384	4	...	✓	0.31
282	2	$03^h20^m28\overset{s}{.}066$	$+00°31'26\overset{''}{.}50$	19.71	0.378	4	...	✓	0.32
238	3	$03^h20^m25\overset{s}{.}962$	$+00°32'58\overset{''}{.}63$	20.62	0.379	4	...	✓	0.35
320	2	$03^h20^m29\overset{s}{.}449$	$+00°31'14\overset{''}{.}78$	20.28	0.374	4	...	✓	0.36
251	3	$03^h20^m26\overset{s}{.}561$	$+00°31'33\overset{''}{.}46$	21.44	0.384	4	✓	✓	0.36
303	3	$03^h20^m28\overset{s}{.}853$	$+00°31'08\overset{''}{.}07$	20.42	0.387	4	...	✓	0.40
271	1	$03^h20^m27\overset{s}{.}617$	$+00°33'34\overset{''}{.}10$	20.30	0.375	4	...	✓	0.40
272	2	$03^h20^m27\overset{s}{.}678$	$+00°33'35\overset{''}{.}89$	20.21	0.375	4	...	✓	0.41
262	2	$03^h20^m27\overset{s}{.}178$	$+00°33'55\overset{''}{.}14$	21.92	0.473	3	✓	...	...
323	1	$03^h20^m29\overset{s}{.}571$	$+00°30'30\overset{''}{.}98$	20.50	0.383	4	...	✓	0.59
368	2	$03^h20^m31\overset{s}{.}339$	$+00°30'27\overset{''}{.}66$	21.22	0.379	3	✓	✓	0.62
376	3	$03^h20^m31\overset{s}{.}809$	$+00°30'28\overset{''}{.}95$	20.80	0.387	4	...	✓	0.62
421	2	$03^h20^m33\overset{s}{.}887$	$+00°30'42\overset{''}{.}03$	21.36	0.329	4	✓	...	...
375	2	$03^h20^m31\overset{s}{.}666$	$+00°30'03\overset{''}{.}86$	20.37	0.195	4	✓	...	...
348	1	$03^h20^m30\overset{s}{.}356$	$+00°34'47\overset{''}{.}85$	20.64	0.394	4	...	✓	0.75
387	3	$03^h20^m32\overset{s}{.}391$	$+00°30'03\overset{''}{.}50$	20.12	0.381	4	...	✓	0.76
329	1	$03^h20^m29\overset{s}{.}739$	$+00°29'38\overset{''}{.}15$	21.15	0.385	4	...	✓	0.86
427	3	$03^h20^m34\overset{s}{.}181$	$+00°34'56\overset{''}{.}24$	19.36	0.325	4	...	...	...
419	3	$03^h20^m33\overset{s}{.}764$	$+00°29'47\overset{''}{.}60$	22.29	0.374	4	✓	✓	0.87
351	2	$03^h20^m30\overset{s}{.}469$	$+00°29'35\overset{''}{.}85$	21.94	0.383	4	✓	✓	0.88
249	2	$03^h20^m26\overset{s}{.}460$	$+00°29'21\overset{''}{.}87$	22.22	0.326	4	✓	...	...
199	1	$03^h20^m23\overset{s}{.}492$	$+00°35'13\overset{''}{.}97$	21.79	0.483	4	✓	...	...
411	2	$03^h20^m33\overset{s}{.}504$	$+00°35'32\overset{''}{.}84$	18.59	0.183	4	...	...	...
252	3	$03^h20^m26\overset{s}{.}596$	$+00°35'39\overset{''}{.}38$	18.38	0.196	4	...	...	...
98	1	$03^h20^m16\overset{s}{.}227$	$+00°32'05\overset{''}{.}75$	21.33	0.369	4	...	...	...
236	2	$03^h20^m25\overset{s}{.}752$	$+00°28'40\overset{''}{.}00$	20.47	0.390	4	...	...	...
364	1	$03^h20^m31\overset{s}{.}016$	$+00°28'32\overset{''}{.}55$	19.95	0.391	4	...	...	...
246	2	$03^h20^m26\overset{s}{.}385$	$+00°28'21\overset{''}{.}69$	22.24	0.393	4	✓	...	...

Table A5: Spectroscopic redshifts of galaxies in the direction of ACT-CL J0342.7-0017 measured using SALT RSS; see Table A1 for an explanation of the table columns.

ID	Mask	RA (J2000)	Dec. (J2000)	m_r	z	Q	Em. Lines?	Member?	r (Mpc)
413	1	$03^h42^m44^s\!.804$	$-00°17'18''\!.92$	20.25	0.301	4	✓	✓	0.04
432	1	$03^h42^m45^s\!.707$	$-00°17'37''\!.69$	20.47	0.166	4	...	...	...
362	1	$03^h42^m42^s\!.346$	$-00°17'01''\!.28$	20.58	0.305	4	...	✓	0.16
364	1	$03^h42^m42^s\!.414$	$-00°16'42''\!.67$	20.21	0.304	4	...	✓	0.22
409	1	$03^h42^m44^s\!.651$	$-00°18'14''\!.94$	19.81	0.311	4	...	✓	0.23
474	1	$03^h42^m47^s\!.751$	$-00°17'51''\!.14$	20.56	0.165	4	...	...	...
429	1	$03^h42^m45^s\!.595$	$-00°16'22''\!.35$	21.00	0.311	4	...	✓	0.29
374	1	$03^h42^m42^s\!.883$	$-00°16'09''\!.36$	20.86	0.301	4	✓	✓	0.34
407	1	$03^h42^m44^s\!.546$	$-00°18'40''\!.94$	20.95	0.302	4	...	✓	0.35
363	1	$03^h42^m42^s\!.387$	$-00°15'54''\!.14$	20.23	0.557	4	...	...	...
400	1	$03^h42^m44^s\!.194$	$-00°15'36''\!.13$	20.57	0.238	4	✓	...	...
473	1	$03^h42^m47^s\!.601$	$-00°19'18''\!.95$	20.62	0.286	4	✓	...	...
436	1	$03^h42^m45^s\!.840$	$-00°15'18''\!.69$	19.50	0.239	4	...	...	...
216	1	$03^h42^m35^s\!.633$	$-00°18'02''\!.22$	20.77	0.366	4	✓	...	...
428	1	$03^h42^m45^s\!.590$	$-00°19'50''\!.29$	20.61	0.112	4	✓	...	...
260	1	$03^h42^m37^s\!.754$	$-00°19'30''\!.24$	19.15	0.303	4	...	✓	0.71
274	1	$03^h42^m38^s\!.579$	$-00°15'00''\!.56$	20.70	0.019	3	...	...	...
430	1	$03^h42^m45^s\!.654$	$-00°20'12''\!.98$	20.77	0.309	4	...	✓	0.76
468	1	$03^h42^m47^s\!.405$	$-00°20'24''\!.07$	19.67	0.366	4	...	...	...
498	1	$03^h42^m48^s\!.728$	$-00°20'44''\!.52$	20.80	0.287	4	✓	...	...
521	1	$03^h42^m50^s\!.300$	$-00°20'58''\!.49$	21.30	0.462	4	...	...	...

Table A6: Spectroscopic redshifts of galaxies in the direction of ACT-CL
J0348.6-0028 measured using SALT RSS; see Table A1 for an explanation of the table columns.

ID	Mask	RA (J2000)	Dec. (J2000)	m_r	z	Q	Em. Lines?	Member?	r (Mpc)
252	4	$03^h48^m38\overset{s}{.}726$	$-00°28'07\overset{''}{.}42$	18.13	0.138	4	...	...	...
246	1	$03^h48^m38\overset{s}{.}378$	$-00°28'23\overset{''}{.}21$	20.49	0.344	4	...	✓	0.09
274	3	$03^h48^m39\overset{s}{.}545$	$-00°28'16\overset{''}{.}90$	19.22	0.345	4	...	✓	0.10
229	4	$03^h48^m37\overset{s}{.}682$	$-00°28'20\overset{''}{.}77$	20.07	0.139	4	...	...	...
218	2	$03^h48^m37\overset{s}{.}125$	$-00°27'48\overset{''}{.}38$	18.17	0.160	4	...	...	...
230	1	$03^h48^m37\overset{s}{.}699$	$-00°28'36\overset{''}{.}14$	20.40	0.342	4	...	✓	0.16
207	1	$03^h48^m36\overset{s}{.}300$	$-00°27'49\overset{''}{.}82$	20.50	0.340	4	...	✓	0.18
232	3	$03^h48^m37\overset{s}{.}909$	$-00°28'46\overset{''}{.}75$	21.04	0.345	3	...	✓	0.21
219	1	$03^h48^m37\overset{s}{.}131$	$-00°27'25\overset{''}{.}16$	20.84	0.325	3	...	...	...
303	1	$03^h48^m41\overset{s}{.}534$	$-00°28'07\overset{''}{.}50$	19.87	0.344	4	...	✓	0.22
304	2	$03^h48^m41\overset{s}{.}593$	$-00°27'35\overset{''}{.}15$	19.48	0.547	4	...	...	...
215	1	$03^h48^m36\overset{s}{.}792$	$-00°27'12\overset{''}{.}79$	20.54	0.350	4	...	✓	0.29
264	1	$03^h48^m39\overset{s}{.}134$	$-00°29'05\overset{''}{.}30$	21.02	0.350	4	...	✓	0.30
315	3	$03^h48^m42\overset{s}{.}291$	$-00°28'29\overset{''}{.}17$	21.08	0.349	4	...	✓	0.30
312	1	$03^h48^m42\overset{s}{.}151$	$-00°28'48\overset{''}{.}76$	19.76	0.346	4	...	✓	0.34
239	1	$03^h48^m38\overset{s}{.}081$	$-00°29'18\overset{''}{.}25$	20.68	0.348	4	...	✓	0.36
165	3	$03^h48^m33\overset{s}{.}621$	$-00°28'04\overset{''}{.}90$	20.68	0.345	4	...	✓	0.36
308	3	$03^h48^m42\overset{s}{.}024$	$-00°28'58\overset{''}{.}10$	21.09	0.342	4	...	✓	0.37
255	4	$03^h48^m38\overset{s}{.}949$	$-00°26'50\overset{''}{.}01$	21.29	0.344	4	...	✓	0.37
330	3	$03^h48^m43\overset{s}{.}143$	$-00°27'31\overset{''}{.}36$	20.92	0.345	4	...	✓	0.38
237	1	$03^h48^m37\overset{s}{.}972$	$-00°26'40\overset{''}{.}69$	20.56	0.346	4	...	✓	0.42
181	4	$03^h48^m34\overset{s}{.}662$	$-00°29'07\overset{''}{.}57$	21.34	0.357	4	...	...	...
272	2	$03^h48^m39\overset{s}{.}430$	$-00°26'39\overset{''}{.}99$	20.69	0.180	3	✓	...	...
324	3	$03^h48^m42\overset{s}{.}877$	$-00°27'08\overset{''}{.}04$	22.05	0.325	4	...	...	...
350	1	$03^h48^m44\overset{s}{.}405$	$-00°27'37\overset{''}{.}55$	20.98	0.340	4	...	✓	0.46
153	2	$03^h48^m32\overset{s}{.}984$	$-00°27'17\overset{''}{.}87$	22.25	0.489	3	...	...	...
358	3	$03^h48^m45\overset{s}{.}127$	$-00°27'45\overset{''}{.}73$	20.81	0.291	4	✓	...	...
305	1	$03^h48^m41\overset{s}{.}623$	$-00°26'27\overset{''}{.}56$	20.32	0.183	4	...	...	...
206	1	$03^h48^m36\overset{s}{.}276$	$-00°30'01\overset{''}{.}29$	20.94	0.346	4	...	✓	0.60

Table A6 – continued from previous page

ID	Mask	RA (J2000)	Dec. (J2000)	m_r	z	Q	Em. Lines?	Member?	r (Mpc)
378	4	$03^h48^m46\overset{s}{.}494$	$-00°27'42\overset{''}{.}89$	19.60	0.190	4	...	...	...
169	3	$03^h48^m33\overset{s}{.}978$	$-00°30'01\overset{''}{.}20$	20.46	0.296	4	...	...	...
320	1	$03^h48^m42\overset{s}{.}708$	$-00°25'44\overset{''}{.}78$	20.20	0.360	3	...	...	...
270	4	$03^h48^m39\overset{s}{.}412$	$-00°25'30\overset{''}{.}78$	19.13	0.352	4	...	✓	0.77
98	3	$03^h48^m28\overset{s}{.}95$	$-00°29'10\overset{''}{.}64$	20.20	0.341	4	...	✓	0.78
107	3	$03^h48^m29\overset{s}{.}523$	$-00°29'31\overset{''}{.}57$	20.86	0.308	4	...	...	...
149	4	$03^h48^m32\overset{s}{.}871$	$-00°30'22\overset{''}{.}95$	21.29	0.340	4	...	✓	0.80
231	1	$03^h48^m37\overset{s}{.}854$	$-00°25'21\overset{''}{.}24$	20.67	0.351	4	...	✓	0.81
371	3	$03^h48^m45\overset{s}{.}867$	$-00°30'25\overset{''}{.}66$	21.75	0.334	4	...	...	...
410	3	$03^h48^m49\overset{s}{.}289$	$-00°26'44\overset{''}{.}32$	20.30	0.282	4	✓	...	...
136	1	$03^h48^m32\overset{s}{.}246$	$-00°25'03\overset{''}{.}39$	20.76	0.341	3	...	...	...
258	1	$03^h48^m39\overset{s}{.}012$	$-00°31'35\overset{''}{.}60$	20.27	0.389	4	...	...	...
141	1	$03^h48^m32\overset{s}{.}555$	$-00°31'24\overset{''}{.}45$	19.99	0.295	4	...	...	...
99	3	$03^h48^m29\overset{s}{.}063$	$-00°25'15\overset{''}{.}83$	20.34	0.342	3	...	...	...
401	1	$03^h48^m48\overset{s}{.}183$	$-00°31'03\overset{''}{.}08$	20.82	0.458	4	...	...	...
285	2	$03^h48^m40\overset{s}{.}530$	$-00°24'16\overset{''}{.}09$	21.34	0.379	4	...	...	...
174	2	$03^h48^m34\overset{s}{.}196$	$-00°31'48\overset{''}{.}88$	21.63	0.417	3	✓	...	...

Table A7: Spectroscopic redshifts of galaxies in the direction of ACT-CL J2058.8+0123 measured using SALT RSS; see Table A1 for an explanation of the table columns.

ID	Mask	RA (J2000)	Dec. (J2000)	m_r	z	Q	Em. Lines?	Member?	r (Mpc)
184	1	$20^h58^m53\overset{s}{.}730$	$+01°23'36\overset{''}{.}04$	20.83	0.315	4	...	...	...
194	1	$20^h58^m54\overset{s}{.}089$	$+01°22'24\overset{''}{.}07$	20.71	0.323	3	...	✓	0.17
173	2	$20^h58^m52\overset{s}{.}683$	$+01°22'14\overset{''}{.}21$	19.86	0.204	4	...	...	...
219	2	$20^h58^m56\overset{s}{.}777$	$+01°22'47\overset{''}{.}58$	19.66	0.338	4	...	...	...
157	2	$20^h58^m51\overset{s}{.}547$	$+01°23'54\overset{''}{.}82$	21.00	0.326	4	...	✓	0.29
177	1	$20^h58^m53\overset{s}{.}056$	$+01°24'10\overset{''}{.}76$	18.13	0.330	4	...	✓	0.33
137	3	$20^h58^m50\overset{s}{.}390$	$+01°23'56\overset{''}{.}26$	19.60	0.327	4	...	✓	0.34

Table A7 – continued from previous page

ID	Mask	RA (J2000)	Dec. (J2000)	m_r	z	Q	Em. Lines?	Member?	r (Mpc)
164	2	$20^h58^m52\overset{s}{.}060$	$+01°21'40\overset{''}{.}62$	19.50	0.333	4	...	✓	0.39
200	1	$20^h58^m54\overset{s}{.}514$	$+01°24'26\overset{''}{.}77$	20.55	0.332	4	...	✓	0.40
225	3	$20^h58^m57\overset{s}{.}187$	$+01°21'51\overset{''}{.}00$	19.72	0.321	4	...	✓	0.41
166	2	$20^h58^m52\overset{s}{.}163$	$+01°24'30\overset{''}{.}79$	20.38	0.324	4	...	✓	0.43
162	2	$20^h58^m51\overset{s}{.}745$	$+01°24'45\overset{''}{.}88$	20.97	0.328	4	...	✓	0.51
211	1	$20^h58^m55\overset{s}{.}861$	$+01°21'03\overset{''}{.}94$	20.73	0.327	3	...	✓	0.57
201	2	$20^h58^m54\overset{s}{.}572$	$+01°20'59\overset{''}{.}56$	20.54	0.329	4	...	✓	0.57
190	1	$20^h58^m53\overset{s}{.}906$	$+01°25'24\overset{''}{.}84$	19.60	0.186	4	✓	...	...
213	1	$20^h58^m56\overset{s}{.}096$	$+01°20'41\overset{''}{.}27$	20.44	0.329	4	...	...	...
203	2	$20^h58^m54\overset{s}{.}836$	$+01°20'35\overset{''}{.}18$	18.00	0.331	4	✓	...	...
146	2	$20^h58^m50\overset{s}{.}917$	$+01°25'22\overset{''}{.}66$	19.69	0.323	4	✓	✓	0.69
90	3	$20^h58^m46\overset{s}{.}076$	$+01°24'52\overset{''}{.}59$	18.14	0.293	4	✓	...	...
153	1	$20^h58^m51\overset{s}{.}408$	$+01°25'57\overset{''}{.}05$	19.66	0.332	4	...	✓	0.83
136	1	$20^h58^m50\overset{s}{.}317$	$+01°26'09\overset{''}{.}59$	21.34	0.325	4	✓	✓	0.91
165	3	$20^h58^m52\overset{s}{.}163$	$+01°26'23\overset{''}{.}63$	17.86	0.134	4	...	...	...
210	2	$20^h58^m55\overset{s}{.}832$	$+01°26'29\overset{''}{.}51$	20.27	0.135	4	...	...	...
150	1	$20^h58^m51\overset{s}{.}379$	$+01°19'14\overset{''}{.}61$	19.92	0.322	4	✓	...	...

A.2 PySALT Processing

PYSALT is a suite of PYRAF tools for the reduction and analysis of data obtained from the RSS instrument mounted on SALT. More information on PySALT can be found in (Crawford et al., 2010). It is important to note that the following methodology/instructions are installation dependent and not universal; some of the settings and options may change over time. It is also worth noting that in the case of SALT RSS spectra some parameters have been carefully derived and should be fixed parameters. Those parameters are listed in the SALT data reduction wiki. The package can be loaded by starting PYRAF. We will now go through each step of the PYSALT data pipeline. The packages can be loaded by starting PYRAF in the terminal (for convention,

the "->" symbol means the terminal prompt):

->pyraf

And we want to enter the PySALT package:

->pysalt

From here we want to go into the 'saltred' (SALT reduction) package.

->saltred

If the package has successfully been installed, you should see the pysalt and saltred packages load and print out onto the screen. All of the tasks can be run from the command line or from 'epar' (edit parameters) and then executed. Using the 'epar' command and then the task name will bring up a GUI interface to use and see the various parameters for the given task. Help files are also available for each of the tasks as well and can be found in the GUI. The first step is to prepare the raw data. This tasks checks for necessary keywords and adds them. These keywords are not written to the file at the telescope but are required in order to improve efficiency in the data reduction pipline and retain consistency with the IRAF-based tools. We use the 'saltprepare' task for this and our settings are as follows:

-> epar saltprepare

saltred - saltprepare task		
Parameter:	Setting:	Description:
images	"P*.fits"	Input raw images or list of images
outimages	""	Output images or list of output images
outpref	"p"	Prefix for output images
createvar	no	Create Variance Frame?
badpixelimag	""	Badpixel image?
clobber	yes	Overwrite existing files?
logfile	"salt.log"	Logfile
verbose	yes	Would you like to see script output?
mode	"al"	

The next step is to correct for the gain of the different CCDs. The RSS instrument has a three-CCD mosaic. Each amplifier has a specific gain factor which varies slowly over time but which is constant across the amplifiers. Gain values depend on the readout speed and gain setting of the CCD. For all possible permutations, gains are stored in an ascii table which is updated

periodically. The saltgain task extracts gains from the ascii table and applies them to raw data. We use the task 'saltgain' to perform this correction:

-epar saltgain

saltred - saltgain task		
Parameter:	Setting:	Description:
images	"pP*.fits"	Input raw images or list of images
outimages	""	Output images or list of output images
outpref	"g"	Prefix for output images
gaindb	"your/filepath.dat"	Gain data from database in given location
usedb	yes	Use gain database?
mult	yes	Multiply images by gains?
clobber	yes	Overwrite existing files?
logfile	"salt.log"	Logfile
verbose	yes	Verbose?
mode	"al"	

The next step is to correct for amplifier crosstalk. Each SALTICAM and RSS CCD has two readout amplifiers. There is crosstalk between them at the level of 0.1% which results in faint ghost sources across the image. Ghosts appear as faint mirror images across amplifier boundaries of bright sources. Provided images are not saturated or non-linear, crosstalk can be mostly removed by simple subtraction of a scaled image of one amplifier from its neighbour. The scaling facrtors are supplied as an ascii table through the xtalkfile argument or in the header keywords. To perform this correction we use the 'saltxtalk' task. The parameters used are as follows:

-> epar saltxtalk

The next step is to create a bias frame and subtract the bias from the images. Since the 'saltbias' task performs two separate functions it must be called twice to perform them both. Firstly, saltbias can create a master bias frame. This is typically an average of multiple bias images which have been subtracted by the row-dependent overscan level and trimmed in size by the removal of the overscan region itself. Secondly saltbias will debias science and calibration images using a combination of overscan and masterbias subtraction. To correct for CCD bias we only used the overscan region at the time.

54

saltred - saltxtalk task		
Parameter:	Setting:	Description:
images	”g*.fits”	Input images or list of images
outimages	””	output images or list of output images
outpref	”x”	prefix for output images
xtalkfile	””	crosstalk coefficient data
logfile	”salt.log”	Logfile
usedb	no	Use xtalkfile
clobber	no	Overwrite existing files?
verbose	yes	Verbose?
mode	”al”	

-> epar saltbias

saltred - saltbias task		
Parameters:	Setting:	Description:
images	”x*.fits”	Input images or list of images
outimages	””	output images or list of output images
outpref	”b”	Prefix for output images
subover	yes	Subtract overscan region?
trim	yes	Trim underscan and overscan?
subbias	no	subtract master bias frame?
masterbias	”bias.fits”	Master bias frame
median	no	Use median instead of mean in image statistics?
function	”polynomial”	Overscan fit function
order	3	Polynomial order for overscan fit
rej_lo	3.0	Low rejection threshold (sigma) for overscan fit
rej_hi	3.0	High rejection threshold (sigma) for overscan fit
niter	10	Number of rejection iterations for overscan fit
plotover	no	Plot overscan fit?
turbo	no	Fast SLOT mode reduction?
clobber	no	Overwrite existing files?
logfile	”salt.log”	Logfile
verbose	yes	Verbose?
mode	”al”	

The next task, 'saltcrclean', cleans multiple CCD extensions of cosmic rays. This task is capable of cleaning cosmic rays from single or multi-extension fits data. The task gives users a choice of three different methods of cleaning cosmic rays that profice different levels of perfor-

mance. The three choices the user has are between fast, median, and edge cosmic ray detection. For our purposes we used 'fast'.

saltred - saltcrclean task		
Parameters:	Setting:	Description:
images	"b*.fits"	Input images or list of images
outimages	""	output images or list of output images
outpref	"c"	Prefix for output images
crtype	"fast"	Type of cosmic ray cleaning
thres	5.0	Threshold above sigma for cosmic ray detection
mbox	5	Window size for searching for cosmic rays
bthresh	3.0	Threshold for sigma clipping background
flux_ratio	0.2	Flux ratio to identify cosmic rays (fast only)
bbox	11	Window size for background statistics (median only)
gain	1.0	Gain of the image (edge only)
rdnoise	5.0	Readnoise of the image (edge only)
fthresh	5.0	Threshold for excluding compact sources (edge only)
bfactor	2	Factor to sub-pixel sample the images (edge only)
gbox	3	Window size to grow; gbox = 0 for no growth of cosmic rays
maxiter	5	Max number of iterations to search for cosmic rays
multithread	no	Use multithreading to process the data?
clobber	no	Overwrite existing files?
logfile	"salt.log"	Logfile
verbose	yes	Verbose?
mode	"al"	

Next we want to apply a flatfield correction but to do this we need to create a master flatfield. We will use the task 'saltcombine' to put together the five flatfields we have to create a master-flat. The separate flatfield images will come with the rest of your raw data. The flatfields have gone through all the previous steps (along with your science and calibration files). To run a list of images you need to put '@' before the file list name. The settings we used in 'saltcombine' are below:

-> epar saltcombine

Before we can use the master flat we need to apply an illumination correction to it. This can be done using the 'saltillum' task.

-epar saltillum

56

saltred - saltcombine task		
Parameters:	Settings:	Description:
images	"@flat_list.txt"	Input images or list of images
outimages	"master_flat.fits"	output images or list of output images
combine	"average"	Type of combine operation
reject	"None"	Type of rejection
mask	no	Use BPM Frame in combining the data
weight	no	Use Inverse Variance frames as weights
blank	0.0	Value if there are no pixels
scale	"None"	Method for scaling the images
statsec	""	Image section for computing statistics
lthresh		Lower Threshold
hthresh		Upper Threshold
clobber	no	Overwrite existing files?
logfile	"salt.log"	Logfile
verbose	yes	Verbose?
mode	"al"	

saltred - saltillum task		
Parameters:	Settings:	Description:
images	"master_flat.fits"	Input images
outimages	""	Output images or list of output images
outpref	"illum"	Prefix for output images
mbox	11	Median smoothing box size
clobber	yes	Overwrite existing files?
logfile	"salt.log"	Logfile
verbose	yes	Verbose?
mode	"al"	

Once this task is complete we can apply the illumination-corrected master flat to the rest of the data (only needed on the science and calibration files). We will use the task 'saltflat'. This task will correct SALT images for flatfield variations.

->epar saltflat

Raw SALT data is stored in FITS files using separate file extensions for each amplifier image. Each CCD has two redout amplifiers and each detector has multiple CCDs. Hence a single RSS exposure is stored in a 2x3 FITS extension. The 'saltmosaic' task combines a set of amplifier images, obtained during the same exposure, into a single mosaiced image, sorted in a single

saltred - saltflat task		
Parameters:	Settings:	Description:
images	"cbxgpP..."	Input images
outimages	""	Output images or list of output images
outpref	"f"	Prefix for output images
flatimage	"illumaster_flat.fits"	Flatfield image
minflat	1.0	Minimum flatfield value
allext	yes	Normalize using all extensions
clobber	yes	Overwrite existing files?
logfile	"salt.log"	Logfile
verbose	yes	Verbose?
mode	"al"	

extension of the output FITS file. Saltmosaic task performs its task in three steps: (1) For each CCD in the array, stitch the two amplifiers together (2) rotate and translate CCD images with respect to the reference CCD using the data stored in the geometry file, "geomfile" (this is located within the pysalt/data/rss/ filepath when PySALT is installed) (3) For each exposure, stitch the CCDs together to form a single image, written to a file with the specified output name. The task settings for 'saltmosaic' are as follows:

-> epar saltmosaic

saltred - saltmosaic task		
Parameters:	Settings:	Description:
images	"fcbxgpP..."	Input images
outimages	""	Output images or list of output images
outpref	"m"	Prefix for output images
geomfile	"/file/path/RSSgeom.dat"	File path to CCD geometry definition file
interp	"linear"	Pixel interpolation function
logfile	"salt.log"	Logfile
geotran	yes	Use geotran for transforming files?
cleanup	yes	Delete temporary files?
clobber	yes	Overwrite existing files?
verbose	yes	Verbose?
mode	"al"	

This marks the end of all the tasks needed in the 'saltred' package. We now need to switch to the 'saltspec' (SALT spectroscopy) package. We will be using the 'specslit' task within the

saltspec package. This task allows us to separate each aperture in the multi-object spectoscopy image into a separate image extension. The slitfile that is needed to run this task is located on the SALT WebManager. From the WebManager you need to select your project, night of observation, and specific mask (in our case). Go to the RSS Science Configuration section and there will be a link that says, "Download XML". For the given object you can copy the contents of that page into a .xml file and save it as your slitmask_whatever.xml file.

-> epar specslit

saltspec - specslit task		
Parameters:	Settings:	Description:
images	"mfcbxgpP..."	Input images
outimages	""	Output images or list of output images
outpref	"s"	Prefix for output images
exttype	"rsmt"	Type of extraction file, RSMT, FITS, ASCII, AUTO
slitfile	"slitmask2.xml"	RSMT, FITS or ASCII file to be used for slit detection
outputslitfile	"mask2"	Output ASCII file that contains slit positions
sections	3	Image sections used to sum up columns. Not smaller than 3.
width	25.0	Width in pixels of Gaussian convolved with edge detected array
sigma	2.2	Sigma used for Gaussian convolution of edge detected array
thres	6.0	Threshold used for edge detection
order	2	Order used for spline fitting
padding	5	Padding to extracted slits
yoffset	-12.0	Offset between mask center and center of CCD
inter	yes	Plot the detected slits on the screen for inspection by user
clobber	yes	Overwrite existing files
logfile	"salt.log"	Logfile
verbose	yes	If verbose=n, log messages will be suppressed.
mode	"al"	

This marks the end of the tools used in PySALT for the basic processing. Now we will move onto the IRAF tasks that were used for processing.

A.3   IRAF Processing

IRAF tasks are used to determine a wavelength dispersion function from a calibration lamp (Xenon or Argon), fit and transform the arc dispersion to the science frames, apply a background

subtraction of a constant value determined locally within each slitlet, combine images (where available), and extract one dimensional sums across the apertures. We will now go through each step of the IRAF data pipeline. It is important to look at your images after each step of the process (if applicable) in Ds9 or something similar. You do not want to get to the end to find a skewed spectrum and then have to guess where it went wrong. The packages can be loaded by starting IRAF in the terminal (for convention, the '->' symbol means the terminal prompt). Most of the tasks we need are located inside the NOAO - TWODSPEC - LONGSLIT package; we will start there.

-> ecl -> noao -> twodspec -> longslit

The first task we will use is 'identify'. This will be run on your calibration images (your reference lamps images). This task is used to: measure positions of features in an image, determine dispersion solutions for spectra, and to identify features in two and three dimensional coordinate transformation. Features in the input images (the calibration images) are identified interactively and the features are assigned coordinates by the user. A coordinate function is created from the identified features that maps pixel coordinates to the 'user coordinates'. A 'user coordinate' list may be defined to automatically identify additional features (this is typically a line list). This task is changing your calibration image from pixel space to wavelength space. Note: it is important the spectrum of the calibration lamp is extracted the same way as the one of the object frame so the calibration is applicable.

->epar identify

The next task we will use is 'reidentify'. This task is used for transferring dispersion solutions in the calibration spectra (the one that was just identified) and for mapping the dispersion distortion in the two dimensional image. Reidentify takes the initial dispersion solution you just found in one line (middle line) with the 'identify' task and extends (in vertical space) that fit over the entire spatial dimension of the image (by step size set in settings).

If you've run reidentify interactively you will be prompted to adjust the dispersion calculated in the new line. You can look at the RMS value of the new dispersion and decide or not whether to adjust it. If you decide yes it will take you back to and 'identify' looking GUI for you to mark features and adjust the dispersion solution. You will be prompted as many times as the number

longslit - identify		
Parameters:	Settings:	Description:
images	calibration_file.fits	Images containing features to be identified
section	middle line	Section to apply to two dimensional images
database	database	Database in which to record feature data
coordlist	argon_lines.txt	User coordinate list
units	””	Coordinate units
nsum	10	Number of lines/columns/bands to sum in 2D images
match	-3.	Coordinate list matching limit
maxfeat	50	Maximum number of features for automatic identification
zwidth	100.	Zoom graph width in user units
ftype	emission	Feature type
fwidth	7.5	Feature width in pixels
cradius	5.	Centering radius in pixels
thresho	10.	Feature threshold for centering
minsep	2.	Minimum pixel separation
functio	spline3	Coordinate function
order	1	Order of coordinate function
sample	*	Coordinate sample regions
niterat	1	Rejection iterations
low_rej	3.	Lower rejection sigma
high_re	3.	Upper rejection sigma
grow	0.	Rejection growing radius
autowri	no	Automatically write to database
graphic	stdgraph	Graphics output device
cursor	””	Graphics cursor input
crval	””	Approximate coordinate (at reference pixel)
cdelt	””	Approximate dispersion
aidpars	””	Automatic identification algorithm parameters
mode	ql	

of steps you have chosen. The number of lines you sum in the ”nsum” parameter can save you a lot of toil. It sums that number of lines together to search for features. Parameters like step and nsum can be changed depending on how much curvature is in your image (step) and how much signal is in your spectrum (nsum). If there is a lot of curvature you want a smaller step value so you can sample the vertical space of the spectrum more often - this information will be used later to straighten out the curve. If your signal is weak you can use the ”nsum” parameter to stack multiple lines together to build up signal, making it easier to identify features.

longslit - reidentify		
Parameters:	Settings:	Description:
referenc	calibration_file.fits	Reference image
images	calibration_file.fits	Images to be reidentified
(interac	yes	Interactive fitting?
(section	middle line	Section to apply to two dimensional images
(newaps	yes	Reidentify apertures in images not in reference?
(overrid	no	Override previous solutions?
(refit	no	Refit coordinate function?
(trace	yes	Trace reference image?
(step	3	Step in lines/columns/bands for tracing an image
(nsum	10	Number of lines/columns/bands to sum
(shift	INDEF	Shift to add to reference features (INDEF to search)
(search	100.	Search radius
(nlost	20	Maximum number of features which may be lost
(cradius	5.	Centering radius
(thresho	0.	Feature threshold for centering
(addfeat	yes	Add features from a line list?
(coordli	argon_lines.txt	User coordinate list
(match	-3.	Coordinate list matching limit
(maxfeat	50	Maximum number of features for automatic identification
(minsep	2.	Minimum pixel separation
(databas	database	Database
(logfile	logfile	List of log files
(plotfil	””	Plot file for residuals
(verbose	yes	Verbose output?
(graphic	stdgraph	Graphics output device
(cursor	””	Graphics cursor input
answer	yes	Fit dispersion function interactively?
crval	””	Approximate coordinate (at reference pixel)
cdelt	””	Approximate dispersion
(aidpars	””	Automatic identification algorithm parameters
(mode	al	

Fitcoords

After the reidentify task we will run the 'fitcoords' task. This task is run on the calibration file that you just processed through identify and reidentify. This task takes the feature coordinates determined by the user from the previous steps and maps them to the image's coordinates.

-epar fitcoords

longslit - fitcoords		
Parameters:	Settings:	Description:
images	lamp.file	Images whose coordinates are to be fit
fitname	””	Name for coordinate fit in the database
interac	yes	Fit coordinates interactively?
combine	no	Combine input coordinates for a single fit?
databas	database	Database
deletion	deletions.db	Deletion list file (not used if null)
function	legendre	Type of fitting function
xorder	5	X order of fitting function
yorder	3	Y order of fitting function
logfile	STDOUT,logfile	Log files
plotfil	plotfile	Plot log file
graphic	stdgraph	Graphics output device
cursor	””	Graphics cursor input
mode	ql	

It is correct to not include the ”.fits” in listing the filename in the images parameter. Running this will open up an interactive window where you can check residuals of your data and fits and if there is any systematics in the data. The graph you first see will be a little intimidating. You can view the data in various ways by typing ’xxyyr’ which is saying x-axis=x, y=axis=y, redraw. Another example is ’xryyr’ which is plotting x-axis=residuals, y-axis-y, redraw. You can do various combinations of plotting schemes to show residuals in either x or y and you can change the function and order of the function (by typing ”func:func order#” in the window). You can delete single points, rows, or columns of data if they are bad. Once you are satisfied you can press ’q’ and it will write out the solution to your database.

Now that we have a solution that maps the users coordinates (which were marked in wavelength) to the image’s coordinates (of pixels) we want to use the task ’transform’ to transform the science images (that are in pixel space) to the user’s coordinates (which are in wavelength space).

-epar transform

NOTE: the parameter ’fitnames’, the names of coordinate fits in the database, has to be the name of the file you created in the previous fitcoords step. It will not have a .fits at the end of it

longslit - transform		
Parameters:	Settings:	Description:
input	science.fits	Input images
output	science.trans.fits	Output images
minput	""	Input masks
moutput	""	Output masks
fitnames	lamp.file	Names of coordinate fits in the database
(databas	database	Identify database
(interpt	linear	Interpolation type
(x1	INDEF	Output starting x coordinate
(x2	INDEF	Output ending x coordinate
(dx	INDEF	Output X pixel interval
(nx	INDEF	Number of output x pixels
(xlog	no	Logarithmic x coordinate?
(y1	INDEF	Output starting y coordinate
(y2	INDEF	Output ending y coordinate
(dy	INDEF	Output Y pixel interval
(ny	INDEF	Number of output y pixels
(ylog	no	Logarithmic y coordinate?
(flux	yes	Conserve flux per pixel?
(blank	INDEF	Value for out of range pixels
(logfile	STDOUT,logfile	List of log files
(mode	ql	

and shouldn't be listed with a .fits in this step. It is very important to do things correctly in the previous steps as any errors will propagate through and your transformations will be wrong.

Now that we have transformed the science image(s) into wavelength space we can subtract the background contamination from the image. What the task background does is remove the skylines from your image. For each line or column in the input images a function is fit to the columns or lines specified by the sample parameter. This function is then subtracted from the entire line or column to create an output line or column. The function fitting parameters may be set interactively. This task is a script using fit1d. For more discussion about the parameters see the help text for icfit and fit1d.

For our specific spectra where the spectrum is horizontal, you will mark out two regions (above and below) where the galaxy spectra lies in the 2-d image. The counts from those two sampled regions will be averaged, meaned, or added to give a single value - that will be the

value subtracted from that given column you chose to look at. You want to chose a function (polynomial, chebyshev, legendre) and two regions above and below the galactic spectrum that gives accurate readings for every column along the image (that means it doesn't sample the galaxy spectra or the sampling region doesn't sample the edge of the image which is 0 and could throw off your average/sum for that column). You'll want to look at different columns of the image to make sure your sample areas are correct, for example looking at column 0, 100, 500, 1000, 2000, 3100, etc. This function and these sampling regions will be applied to every column in our 2-d image (in our case there is 3175 columns). The point of fitting the background is to trace the strength of the flux of the sky lines as they span the chip. You want to be able to use a consistent measuring tool across every column and therefore it'll apply the same method across varying amounts of background. For example if it comes across a bright sky line you want it to subtract more from that column than the other column without any sky lines. The way you measure the counts for that column will be consistent but the counts themselves will not be the same. This will insure you are extracting the maximum amount of real signal from your image.

-> epar transform

longslit - background		
Parameters:	Settings:	Description:
input	science.trans.fits	Input images to be background subtracted
output	science.tran_back.fits	Output background subtracted images
(axis	2	Axis along which background is fit and subtracted
(interac	yes	Set fitting parameters interactively?
(sample	*	Sample of points to use in fit
(naverag	1	Number of points in sample averaging
(functio	legendre	Fitting function
(order	1	Order of fitting function
(low_rej	3.	Low rejection in sigma of fit
(high_re	3.	High rejection in sigma of fit
(niterat	5	Number of rejection iterations
(grow	0.	Rejection growing radius
(graphic	stdgraph	Graphics output device
(cursor	""	Graphics cursor input
(mode	ql	

If you have multiple exposures of the same object you can combine them after all the other

previous steps have been performed to increase signal strength. This task is called 'imcombine' (image combine). Images are combined by weighted averaging, medianing, or summing. Pixels may be rejected from the combining by using pixel masks, threshold levels, and rejection algorithms (this can be exploited to remove any left-over cosmic ray contamination).That can be done by adjusting 'hthreshold' values - it adjusts the level of allowed pixels with certain strengths. The images may be scaled, before rejections, multiplicatively, additively, or both based on image statistics, image header keywords, or text files. The images may be combined with integer pixel coordinate offsets. You need to list each image in the input parameter seperated by a comma.

-epar imcombine

We are now ready to extract the processed spectrum. For the next and final step we will have to switch packages. We will be running the 'apall' (aperture all) task from the noao - twodspec - apextract package. This is a task that has a lot of functionality which we will not be going into. There are many manuals online that can describe it to the full extent but we will only be concerned with the settings for our specific data. We will be using it to extract one dimensional sums across our 2-d image. What that means is we will it the number of lines our galaxy spectrum spans (remember, our spectrum is horizontal), say rows 15-25 of the full image width of 0-40 rows, and it will sum up the counts between row 15-25 for each column in the image (all 3175 in our case). This will return a "1-dimensional sum" for each column in the image. If you plot this result you will get a plot of your spectrum.

-> noao -> twodspec -> apextract -> epar apall

There are A LOT of settings in apall and it is worth while to read Users Guide to Reducing Slit Spectra with IRAF to understand and tailor the routine to your data. Keep in mind if you want to run this in a script and not interactively a lot of these settings will change. You can check what your spectrum looks like by using the 'splot' command.

A.4   Cross-Correlation

Peaks in the cross-correlation function are identified and fit by a parabola, quartic, or function of the form $\cos(x)(1+x^2)$ to obtain their position and width and hence the redshift and velocity

longslit - imcombine		
Parameters:	Settings:	Description:
input	sci1.fits,sci2.fits	List of images to combine
output	science_combined.fits	List of output images
headers	””	List of header files (optional)
bpmasks	””	List of bad pixel masks (optional)
rejmask	””	List of rejection masks (optional)
nrejmas	””	List of number rejected masks (optional)
expmask	””	List of exposure masks (optional)
sigmas	””	List of sigma images (optional)
imcmb	$I	Keyword for IMCMB keywords
logfile	STDOUT	Log file
combine	median	Type of combine operation
reject	sigclip	Type of rejection
project	no	Project highest dimension of input images?
outtype	real	Output image pixel datatype
outlimi	””	Output limits (x1 x2 y1 y2 ...)
offsets	none	Input image offsets
masktyp	none	Mask type
maskval	0	Mask value
blank	0.	Value if there are no pixels
scale	none	Image scaling
zero	none	Image zero point offset
weight	none	Image weights
statsec	””	Image section for computing statistics
expname	””	Image header exposure time keyword
lthresh	INDEF	Lower threshold
hthresh	100	Upper threshold
nlow	1	minmax: Number of low pixels to reject
nhigh	1	minmax: Number of high pixels to reject
nkeep	1	Minimum to keep (pos) or maximum to reject (neg)
mclip	yes	Use median in sigma clipping algorithms?
lsigma	3.	Lower sigma clipping factor
hsigma	3.	Upper sigma clipping factor
rdnoise	0.	ccdclip: CCD readout noise (electrons)
gain	1.	ccdclip: CCD gain (electrons/DN)
snoise	0.	ccdclip: Sensitivity noise (fraction)
sigscal	0.1	Tolerance for sigma clipping scaling corrections
pclip	-0.5	pclip: Percentile clipping parameter
grow	0.	Radius (pixels) for neighbor rejection
mode	ql	

dispersion of the galaxy. The fitted parameters are saved, and a summary output is produced for each object. In this summary, the redshift is corrected for the velocity of the template object. The redshift is given as cz in km/sec. The quoted errors are one sigma on each parameter. To do this we used the SDSS DR2 galaxy templates. We used 6 different galaxy templates from SDSS DR2 with which to compare each one of our galaxies to. The steps are as follows:

-> rvsao -> epar xcsao

apextract - apall		
Parameters:	Settings:	Description:
input	science_combined.fits	List of input images
output	science.apall.fits	List of output spectra
apertur	,,,,	Apertures
format	onedspec	Extracted spectra format
referen	,,,,	List of aperture reference images
profile	,,,,	List of aperture profile images
interac	yes	Run task interactively?
find	yes	Find apertures?
recente	yes	Recenter apertures?
resize	no	Resize apertures?
edit	yes	Edit apertures?
trace	yes	Trace apertures?
fittrac	yes	Fit the traced points interactively?
extract	yes	Extract spectra?
extras	yes	Extract sky, sigma, etc.?
review	yes	Review extractions?
line	INDEF	Dispersion line
nsum	100	Number of dispersion lines to sum or median
APERTURE		
lower	-4.	Lower aperture limit relative to center
upper	4.	Upper aperture limit relative to center
apidtab		Aperture ID table (optional)
BACKGROUND		
b_funct	chebyshev	Background function
b_order	1	Background function order
b_sampl	-25:-7,7:25	Background sample regions
b_naver	-100	Background average or median
b_niter	0	Background rejection iterations
b_low_r	3.	Background lower rejection sigma
b_high_	3.	Background upper rejection sigma
b_grow	0.	Background rejection growing radius
CENTERING		
width	8.	Profile centering width
radius	8.	Profile centering radius
thresho	0.	Detection threshold for profile centering
FINDING		
find	,,,,	Number of apertures to be found automatically
minsep	5.	Minimum separation between spectra
maxsep	1000.	Maximum separation between spectra
order	increasing	Order of apertures
RECENTERING		
aprecen	,,,,	Apertures for recentering calculation
npeaks	INDEF	Select brightest peaks
shift	yes	Use average shift instead of recentering?

RESIZING		
llimit	INDEF	Lower aperture limit relative to center
ulimit	INDEF	Upper aperture limit relative to center
ylevel	10.	Fraction of peak or intensity for automatic width
peak	yes	Is ylevel a fraction of the peak?
bkg	yes	Subtract background in automatic width?
r_grow	0.	Grow limits by this factor
avglimi	no	Average limits over all apertures?
TRACING		
t_nsum	10	Number of dispersion lines to sum
t_step	10	Tracing step
t_nlost	3	Number of consecutive times profile is lost before quitting
t_funct	legendre	Trace fitting function
t_order	10	Trace fitting function order
t_sampl	*	Trace sample regions
t_naver	1	Trace average or median
t_niter	1	Trace rejection iterations
t_low_r	3.	Trace lower rejection sigma
t_high_	3.	Trace upper rejection sigma
t_grow	0.	Trace rejection growing radius
EXTRACTION PARAMETERS		
backgro	none	Background to subtract
skybox	1	Box car smoothing length for sky
weights	none	Extraction weights (none—variance)
pfit	fit1d	Profile fitting type (fit1d—fit2d)
clean	no	Detect and replace bad pixels?
saturat	INDEF	Saturation level
readnoi	0.	Read out noise sigma (photons)
gain	1.	Photon gain (photons/data number)
lsigma	4.	Lower rejection threshold
usigma	4.	Upper rejection threshold
nsubaps	1	Number of subapertures per aperture
mode	ql	

rvsao - xcsao		
Parameters:	Settings:	Description:
spectra	spectrum.fits	List of input spectra
specnum	0	Spectrum aperture range if multispec or 2-D file
(specban	0	Spectrum band if multispec file
(specdir	""	Directory for input spectra
(correla	wavelength	Cross-correlate spectrum (velocity wavelength pixel no)
(templat	lrg_temp_lin.fits	List of template spectra
(tempnum	0	Template aperture range if 2-D or multispec file
(tempban	0	Template band if template is multispec file
(tempdir	""	Directory for template spectra
(echelle	no	Echelle spectra (template tracks spectrum) (yes or no)
(st_lamb	5125.	Starting wavelength in Angstroms or pixels to correlate
(end_lam	5780.	Ending wavelength in Angstroms or pixels to correlate
(obj_plo	no	Plot the raw object data
(xcor_pl	no	Plot the filtered correlation function
(xcor_fi	no	Write the filtered correlation function to a file
(fixbad	yes	Eliminate portions of spectrum with bad lines (yes or no)
(badline	badlinestID153.dat	Lines to eliminate from spectrum
(s_emcho	no	Remove emission or absorption lines (yes,no,tempfile)
(t_emcho	no	Remove emission or absorption lines (yes,no,tempfile)
(s_abs_r	100.	Spectrum absorption line rejection in sigma of fit
(s_em_re	2.	Spectrum emission line rejection in sigma of fit
(t_abs_r	100.	Template absorption line rejection in sigma of fit
(t_em_re	2.	Template emission line rejection in sigma of fit
(bell_wi	0.05)	Fraction of spectrum to taper
(renorma	yes	Renormalize spectrum before transform (yes or no)
(ncols	1024	Number of cols into which to rebin
(interp_	spline3)	Rebin interpolation mode
(zeropad	yes	Pad transforms with zeroes to lower noise (yes, no, tempfile)

rvsao - xcsao		(Continued from previous page...)
Parameters:	Settings:	Description:
(low_bin	5	Bin number of low frequency cutoff
(top_low	10	Bin number where low frequency reaches one
(top_nru	80	Bin number where high frequency starts to slope off
(nrun	140	Bin number of high frequency cutoff
(vel_ini	zguess	Initial velocity source (zero guess zguess corr em comb)
(czguess	0.33185	Initial velocity guess in km/sec or z
(nzpass	2	Number of times template is shifted to match object velocity
(tshift	0.	night to night zero point velocity shift
(svel_co	barycentric	Spectrum velocity correction(none,file,helio,bary,hfile)
(tvel_co	none	Template velocity correction (none,file,helio,bary,hfile)
(pkmode	1	Peak-fitting mode (1-parabola 2-quartic 3-cosx/1+x^2)
(pkfrac	0.5	Fraction of peak or number of points for peak fitting (0=FWHM)
(pksrch	25	Half-width of search region for graphically set peak
(minvel	-30000.	Minimum allowable velocity in km/sec
(maxvel	30000.	Maximum allowable velocity in km/sec
(report_	1	Report mode (1=normal 2=one-line)
(logfile	STDOUT,xcsao.log)	List of log files
(save_ve	no	Save result in IRAF data file header (yes or no)
(rvcheck	no	Enable header update if not correlate=no (yes or no)
(archive	no	Save results in binary archive record (yes or no)
(nsmooth	30	Smooth displayed spectrum (0=no else number of times)
(cvel	INDEF	Center velocity of output graph
(dvel	INDEF	Velocity half-width of output graph
(ablines	ablines.dat	Absorption line list

Bibliography

Abazajian, K. N., Adelman-McCarthy, J. K., Agüeros, M. A., Allam, S. S., Allende Prieto, C., An, D., Anderson, K. S. J., Anderson, S. F., Annis, J., Bahcall, N. A., et al., 2009, 'The Seventh Data Release of the Sloan Digital Sky Survey', *ApJS*, 182, 543–558.

Ahn, C. P., Alexandroff, R., Allende Prieto, C., Anders, F., Anderson, S. F., Anderton, T., Andrews, B. H., Aubourg, É., Bailey, S., Bastien, F. A., et al., 2014, 'The Tenth Data Release of the Sloan Digital Sky Survey: First Spectroscopic Data from the SDSS-III Apache Point Observatory Galactic Evolution Experiment', *ApJS*, 211, 17.

Akritas, M. G., Bershady, M. A., 1996, 'Linear Regression for Astronomical Data with Measurement Errors and Intrinsic Scatter', *The Astrophysical Journal*, 470, 706.

Andersson, K., et al., 2011, 'X-Ray Properties of the First Sunyaev-Zel'dovich Effect Selected Galaxy Cluster Sample from the South Pole Telescope', *The Astrophysical Journal*, 738, 48.

Arnaud, M., Pratt, G. W., Piffaretti, R., Böhringer, H., Croston, J. H., Pointecouteau, E., 2010, 'The universal galaxy cluster pressure profile from a representative sample of nearby systems (REXCESS) and the Y_{SZ} - M_{500} relation', *A&A*, 517, A92.

Bahcall, N. A., Fan, X., 1998, 'The Most Massive Distant Clusters: Determining Omega and delta 8', *The Astrophysical Journal*, 504, 1.

Battaglia, N., Bond, J. R., Pfrommer, C., Sievers, J. L., 2012, 'On the Cluster Physics of Sunyaev-Zel'dovich and X-ray Surveys III: Measurement Biases and Cosmological Evolution of Gas and Stellar Mass Fractions', *The Astrophysical Journal*.

Beers, T. C., Flynn, K., Gebhardt, K., 1990, 'Measures of location and scale for velocities in clusters of galaxies - A robust approach', *AJ*, 100, 32–46.

Bonaldi, A., Ricciardi, S., Leach, S., Stivoli, F., Baccigalupi, C., de Zotti, G., 2007, 'WMAP 3-yr data with Correlated Component Analysis: anomalous emission and impact of component separation on the CMB power spectrum', *Monthly Notices of the Royal Astronomical Society*, 382, 1791–1803.

Bonamente, M., Joy, M., LaRoque, S. J., Carlstrom, J. E., Nagai, D., Marrone, D. P., 2008, 'Scaling Relations from Sunyaev-Zel'dovich Effect and Chandra X-Ray Measurements of High-Redshift Galaxy Clusters', *The Astrophysical Journal*, 675, 106–114.

Catala, L., Crawford, S. M., Buckley, D. A. H., Pickering, T. E., Wilson, R. W., Butterley, T., Shepherd, H. W., Marang, F., Matshaya, P., Fourie, C., 2013, 'Optical turbulence characterization at the SAAO Sutherland site', *Monthly Notices of the Royal Astronomical Society*, 436, 590–603.

Crawford, S. M., Still, M., Schellart, P., Balona, L., Buckley, D. A. H., Dugmore, G., Gulbis, A. A. S., Kniazev, A., Kotze, M., Loaring, N., Nordsieck, K. H., Pickering, T. E., Potter, S., Romero Colmenero, E., Vaisanen, P., Williams, T., Zietsman, E., 2010, 'PySALT: the SALT science pipeline', In: Society of Photo-Optical Instrumentation Engineers (SPIE) Conference Series, Vol. 7737 of *Society of Photo-Optical Instrumentation Engineers (SPIE) Conference Series*.

Crawford, S. M., Wirth, G. D., Bershady, M. A., 2014, 'Spatial and Kinematic Distributions of Transition Populations in Intermediate Redshift Galaxy Clusters', *The Astrophysical Journal*, 786, 30.

De Propris, R., et al., 2003, 'The 2dF Galaxy Redshift Survey: the luminosity function of cluster galaxies', *Monthly Notices of the Royal Astronomical Society*, 342, 725–737.

Dressler, A., Shectman, S. A., 1988, 'Evidence for substructure in rich clusters of galaxies from radial-velocity measurements', *AJ*, 95, 985–995.

Duffy, A. R., Schaye, J., Kay, S. T., Dalla Vecchia, C., 2008, 'Dark matter halo concentrations in the Wilkinson Microwave Anisotropy Probe year 5 cosmology', *Monthly Notices of the Royal Astronomical Society*, 390, L64–L68.

Einstein, A., 1916, 'Die Grundlage der allgemeinen Relativitätstheorie', *Annalen der Physik*, 354, 769–822.

Evrard, A. E., Bialek, J., Busha, M., White, M., Habib, S., Heitmann, K., Warren, M., Rasia, E., Tormen, G., Moscardini, L., Power, C., Jenkins, A. R., Gao, L., Frenk, C. S., Springel, V., White, S. D. M., Diemand, J., 2008, 'Virial Scaling of Massive Dark Matter Halos: Why Clusters Prefer a High Normalization Cosmology', *The Astrophysical Journal*, 672, 122–137.

Fadda, D., Girardi, M., Giuricin, G., Mardirossian, F., Mezzetti, M., 1996, 'The Observational Distribution of Internal Velocity Dispersions in Nearby Galaxy Clusters', *The Astrophysical Journal*, 473, 670.

Fowler, J. W., Niemack, M. D., Dicker, S. R., Aboobaker, A. M., Ade, P. A. R., Battistelli, E. S., Devlin, M. J., Fisher, R. P., Halpern, M., Hargrave, P. C., Hincks, A. D., Kaul, M., Klein, J., Lau, J. M., Limon, M., Marriage, T. A., Mauskopf, P. D., Page, L., Staggs, S. T., Swetz, D. S., Switzer, E. R., Thornton, R. J., Tucker, C. E., 2007, 'Optical design of the Atacama Cosmology Telescope and the Millimeter Bolometric Array Camera', 46, 3444–3454.

Friedmann, A., 1924, 'Über die Möglichkeit einer Welt mit konstanter negativer Krümmung des Raumes', *Zeitschrift fur Physik*, 21, 326–332.

Gamow, G., 1948, 'The Origin of Elements and the Separation of Galaxies', *Physical Review*, 74, 505–506.

Guth, A. H., 1981, 'Inflationary universe: A possible solution to the horizon and flatness problems', 23, 347–356.

Haiman, Z., Mohr, J. J., Holder, G. P., 2001, 'Constraints on Cosmological Parameters from Future Galaxy Cluster Surveys', *The Astrophysical Journal*, 553, 545–561.

Hasselfield, M., et al., 2013, 'The Atacama Cosmology Telescope: Sunyaev-Zel'dovich Selected Galaxy Clusters at 148 GHz from Three Seasons of Data', *JCAP submitted (arXiv:1301.0816)*.

Hilton, M., Hasselfield, M., Sifón, C., Baker, A. J., Barrientos, L. F., Battaglia, N., Bond, J. R., Crichton, D., Das, S., Devlin, M. J., Gralla, M., Hajian, A., Hincks, A. D., Hughes, J. P., Infante, L., Irwin, K. D., Kosowsky, A., Lin, Y.-T., Marriage, T. A., Marsden, D., Menanteau, F., Moodley, K., Niemack, M. D., Nolta, M. R., Page, L. A., Reese, E. D., Sievers, J., Spergel, D. N., Wollack, E. J., 2013, 'The Atacama Cosmology Telescope: the stellar content of galaxy clusters selected using the Sunyaev-Zel'dovich effect', *Monthly Notices of the Royal Astronomical Society*, 435, 3469–3480.

Hilton, M., Lloyd-Davies, E., Stanford, S. A., Stott, J. P., Collins, C. A., Romer, A. K., Hosmer, M., Hoyle, B., Kay, S. T., Liddle, A. R., Mehrtens, N., Miller, C. J., Sahlén, M., Viana, P. T. P., 2010, 'The XMM Cluster Survey: Active Galactic Nuclei and Starburst Galaxies in XMMXCS J2215.9-1738 at z = 1.46', *The Astrophysical Journal*, 718, 133–147.

Hubble, E., 1929, 'A Relation between Distance and Radial Velocity among Extra-Galactic Nebulae', *Proceedings of the National Academy of Science*, 15, 168–173.

Kaiser, N., Squires, G., Broadhurst, T., 1995, 'A Method for Weak Lensing Observations', *The Astrophysical Journal*, 449, 460.

Kurtz, M. J., Mink, D. J., 1998, 'RVSAO 2.0: Digital Redshifts and Radial Velocities', *PASP*, 110, 934–977.

Mantz, A., Allen, S. W., Rapetti, D., Ebeling, H., 2010, 'The observed growth of massive galaxy clusters - I. Statistical methods and cosmological constraints', *Monthly Notices of the Royal Astronomical Society*, 406, 1759–1772.

Marriage, T. A., et al., 2011, 'The Atacama Cosmology Telescope: Sunyaev-Zel'dovich-Selected Galaxy Clusters at 148 GHz in the 2008 Survey', *The Astrophysical Journal*, 737, 61.

Marrone, D. P., Smith, G. P., Okabe, N., Bonamente, 2012, 'LoCuSS: The Sunyaev-Zel'dovich Effect and Weak-lensing Mass Scaling Relation', *The Astrophysical Journal*, 754, 119.

Menanteau, F., et al., 2010, 'The Atacama Cosmology Telescope: Physical Properties and Purity of a Galaxy Cluster Sample Selected via the Sunyaev-Zel'dovich Effect', *The Astrophysical Journal*, 723, 1523–1541.

Menanteau, F., et al., 2013, 'The Atacama Cosmology Telescope: Physical Properties of Sunyaev-Zel'dovich Effect Clusters on the Celestial Equator', *The Astrophysical Journal*, 765, 67.

Mosteller, F., Tukey, J. W., 1977, 'Data analysis and regression. A second course in statistics'.

Motl, P. M., Hallman, E. J., Burns, J. O., Norman, M. L., 2005, 'The Integrated Sunyaev-Zeldovich Effect as a Superior Method for Measuring the Mass of Clusters of Galaxies', *ApJL*, 623, L63–L66.

Navarro, J. F., Frenk, C. S., White, S. D. M., 1997, 'A Universal Density Profile from Hierarchical Clustering', *The Astrophysical Journal*, 490, 493.

Okabe, N., Zhang, Y.-Y., Finoguenov, A., Takada, M., Smith, G. P., Umetsu, K., Futamase, T., 2010, 'LoCuSS: Calibrating Mass-observable Scaling Relations for Cluster Cosmology with Subaru Weak-lensing Observations', *The Astrophysical Journal*, 721, 875–885.

Old, L., Gray, M. E., Pearce, F. R., 2013, 'Brighter galaxy bias: underestimating the velocity dispersions of galaxy clusters', *Monthly Notices of the Royal Astronomical Society*, 434, 2606–2615.

Peebles, P. J. E., 1980, 'The large-scale structure of the universe'.

Penzias, A. A., Wilson, R. W., 1965, 'A Measurement of Excess Antenna Temperature at 4080 Mc/s.', *The Astrophysical Journal*, 142, 419–421.

Perlmutter, S., Aldering, G., Goldhaber, G., Knop, R. A., Nugent, P., Castro, P. G., Deustua, S., Fabbro, S., Goobar, A., Groom, D. E., Hook, I. M., Kim, A. G., Kim, M. Y., Lee, J. C., Nunes, N. J., Pain, R., Pennypacker, C. R., Quimby, R., Lidman, C., Ellis, R. S., Irwin, M., McMahon, R. G., Ruiz-Lapuente, P., Walton, N., Schaefer, B., Boyle, B. J., Filippenko, A. V., Matheson, T., Fruchter, A. S., Panagia, N., Newberg, H. J. M., Couch, W. J., Project, T. S. C., 1999, 'Measurements of Ω and Λ from 42 High-Redshift Supernovae', *The Astrophysical Journal*, 517, 565–586.

Polletta, M., Tajer, M., Maraschi, L., Trinchieri, G., Lonsdale, C. J., Chiappetti, L., Andreon, S., Pierre, M., Le Fèvre, O., Zamorani, G., Maccagni, D., Garcet, O., Surdej, J., Franceschini, A., Alloin, D., Shupe, D. L., Surace, J. A., Fang, F., Rowan-Robinson, M., Smith, H. E., Tresse, L., 2007, 'Spectral Energy Distributions of Hard X-Ray Selected Active Galactic Nuclei in the XMM-Newton Medium Deep Survey', *The Astrophysical Journal*, 663, 81–102.

Popesso, P., Böhringer, H., Romaniello, M., Voges, W., 2005, 'RASS-SDSS galaxy cluster survey. II. A unified picture of the cluster luminosity function', *A&A*, 433, 415–429.

Reid, B. A., Spergel, D. N., 2006, 'Sunyaev-Zel'dovich Effect Signals in Cluster Models', *The Astrophysical Journal*, 651, 643–657.

Riess, A. G., Filippenko, A. V., Challis, P., Clocchiatti, A., Diercks, A., Garnavich, P. M., Gilliland, R. L., Hogan, C. J., Jha, S., Kirshner, R. P., Leibundgut, B., Phillips, M. M., Reiss, D., Schmidt, B. P., Schommer, R. A., Smith, R. C., Spyromilio, J., Stubbs, C., Suntzeff, N. B., Tonry, J., 1998, 'Observational Evidence from Supernovae for an Accelerating Universe and a Cosmological Constant', *AJ*, 116, 1009–1038.

Romer, A. K., Viana, P. T. P., Liddle, A. R., Mann, R. G., 2001, 'A Serendipitous Galaxy Cluster Survey with XMM: Expected Catalog Properties and Scientific Applications', *The Astrophysical Journal*, 547, 594–608.

Rozo, E., Wechsler, R. H., Rykoff, E. S., Annis, J. T., Becker, M. R., Evrard, A. E., Frieman, J. A., Hansen, S. M., Hao, J., Johnston, D. E., Koester, B. P., McKay, T. A., Sheldon, E. S., Weinberg, D. H., 2010, 'Cosmological Constraints from the Sloan Digital Sky Survey maxBCG Cluster Catalog', *The Astrophysical Journal*, 708, 645–660.

Sahlén, M., Viana, P. T. P., Liddle, A. R., Romer, A. K., Davidson, M., Hosmer, M., Lloyd-Davies, E., Sabirli, K., Collins, C. A., Freeman, P. E., Hilton, M., Hoyle, B., Kay, S. T., Mann, R. G., Mehrtens, N., Miller, C. J., Nichol, R. C., Stanford, S. A., West, M. J., 2009, 'The XMM Cluster Survey: forecasting cosmological and cluster scaling-relation parameter constraints', *Monthly Notices of the Royal Astronomical Society*, 397, 577–607.

Sehgal, N., et al., 2011, 'The Atacama Cosmology Telescope: Cosmology from Galaxy Clusters Detected via the Sunyaev-Zel'dovich Effect', *The Astrophysical Journal*, 732, 44.

Sifón, C., et al., 2012, 'The Atacama Cosmology Telescope: Dynamical Masses and Scaling Relations for a Sample of Massive Sunyaev-Zel'dovich Effect Selected Galaxy Clusters', *The Astrophysical Journal*.

Smoot, G. F., Bennett, C. L., Kogut, A., Wright, E. L., Aymon, J., Boggess, N. W., Cheng, E. S., de Amici, G., Gulkis, S., Hauser, M. G., Hinshaw, G., Jackson, P. D., Janssen, M., Kaita, E., Kelsall, T., Keegstra, P., Lineweaver, C., Loewenstein, K., Lubin, P., Mather, J., Meyer, S. S., Moseley, S. H., Murdock, T., Rokke, L., Silverberg, R. F., Tenorio, L., Weiss, R., Wilkinson, D. T., 1992, 'Structure in the COBE differential microwave radiometer first-year maps', *ApJL*, 396, L1–L5.

Sofue, Y., Rubin, V., 2001, 'Rotation Curves of Spiral Galaxies', *ARA&A*, 39, 137–174.

Vanderlinde, K., et al., 2010, 'Galaxy Clusters Selected with the Sunyaev-Zel'dovich Effect from 2008 South Pole Telescope Observations', *The Astrophysical Journal*, 722, 1180–1196.

Viana, P. T. P., Liddle, A. R., 1999, 'Galaxy clusters at 0.3¡z¡0.4 and the value of Omega_0', *Monthly Notices of the Royal Astronomical Society*, 303, 535–545.

Vikhlinin, A., Kravtsov, A., Forman, W., Jones, C., Markevitch, M., Murray, S. S., Van Speybroeck, L., 2006, 'Chandra Sample of Nearby Relaxed Galaxy Clusters: Mass, Gas Fraction, and Mass-Temperature Relation', *The Astrophysical Journal*, 640, 691–709.

Vikhlinin, A., et al., 2009, 'Chandra Cluster Cosmology Project III: Cosmological Parameter Constraints', *The Astrophysical Journal*, 692, 1060–1074.

Voit, G. M., 2005, 'Tracing cosmic evolution with clusters of galaxies', *Reviews of Modern Physics*, 77, 207–258.

Wirth, A., Gonsiorowski, T., Roberts, J., Bruno, T. L., Swiegers, J., Gajjar, H., Swat, A., 2004, 'Developing and testing an optical alignment system for SALT"s segmented primary mirror', In: Oschmann, Jr., J. M. (Ed.), Ground-based Telescopes, Vol. 5489 of *Society of Photo-Optical Instrumentation Engineers (SPIE) Conference Series*, pp. 892–902.

Yang, X., Mo, H. J., van den Bosch, F. C., 2008, 'Galaxy Groups in the SDSS DR4. II. Halo Occupation Statistics', *The Astrophysical Journal*, 676, 248–261.

Zehavi, I., Zheng, Z., Weinberg, D. H., Blanton, M. R., Bahcall, N. A., Berlind, A. A., Brinkmann, J., Frieman, J. A., Gunn, J. E., Lupton, R. H., Nichol, R. C., Percival, W. J., Schneider, D. P., Skibba, R. A., Strauss, M. A., Tegmark, M., York, D. G., 2011, 'Galaxy Clustering in the Completed SDSS Redshift Survey: The Dependence on Color and Luminosity', *The Astrophysical Journal*, 736, 59.